

SCIENTIFIC REPORTS

OPEN

The efficacy of Ranolazine on E1784K is altered by temperature and calcium

Mena Abdelsayed, Manpreet Ruprai & Peter C. Ruben

E1784K is the most common mixed syndrome *SCN5a* mutation underpinning both Brugada syndrome type 1 (BrS1) and Long-QT syndrome type 3 (LQT3). The charge reversal mutant enhances the late sodium current (I_{Na}) passed by the cardiac voltage-gated sodium channel ($Na_v1.5$), delaying cardiac repolarization. Exercise-induced triggers, like elevated temperature and cytosolic calcium, exacerbate E1784K late I_{Na} . In this study, we tested the effects of Ranolazine, the late I_{Na} blocker, on voltage-dependent and kinetic properties of E1784K at elevated temperature and cytosolic calcium. We used whole-cell patch clamp to measure I_{Na} from wild type and E1784K channels expressed in HEK293 cells. At elevated temperature, Ranolazine attenuated gain-of-function in E1784K by decreasing late I_{Na} , hyperpolarizing steady-state fast inactivation, and increasing use-dependent inactivation. Both elevated temperature and cytosolic calcium hampered the capacity of Ranolazine to suppress E1784K late I_{Na} . *In-silico* action potential (AP) simulations were done using a modified O'Hara Rudy (ORd) cardiac model. Simulations showed that Ranolazine failed to shorten AP duration, an effect augmented at febrile temperatures. The drug-channel interaction is clearly affected by external triggers, as reported previously with ischemia. Determining drug efficacy under various physiological states in *SCN5a* cohorts is crucial for accurate management of arrhythmias.

The alpha subunit of the cardiac voltage-gated sodium channel, $Na_v1.5$, is encoded by the *SCN5a* gene. Mutations in this gene usually cause long-QT syndrome type 3 (LQT3), Brugada syndrome type 1 (BrS1), or both (mixed syndromes)^{1–5}. These clinical conditions are elicited by expression of gating dysfunctions in $Na_v1.5$ ^{6–10}. Gain- and loss-of-function mutations can modify the inward sodium current (I_{Na}). Gain-of-function (GoF) in $Na_v1.5$ arises from loss in channel fast inactivation, thereby increasing the non-inactivating, late I_{Na} , underlying LQT3^{7,11–16}. Loss-of-function (LoF) mainly arises from decreased peak I_{Na} resulting in BrS1^{1,6,17–20}. Interestingly, both GoF and LoF defects can occur simultaneously in a number of mutants^{6,12,17,21–24}.

A guanine to an adenine substitution at position 5349 in *SCN5a* expresses the charge reversal mutant, E1784K, in the $Na_v1.5$ C-terminal domain (CTD)^{25,26}. E1784K is the most common mixed syndrome mutant, particularly prevalent in the Okinawa Islands in Japan, where carriers mainly express diagnostic LQT3²⁷. Clinical studies reveal differential phenotypic expressivity in E1784K cohorts^{12,22,28,29}.

E1784K is located directly upstream of the acidic globular EF-like hand domain (α_1 – α_4). The residue contributes to the electrostatic interactions formed between the acidic domain and the downstream basic IQ domain (α_6 , Fig. 1 compares WT to E1784K structure)^{30–34}. The proximal CTD, in which E1784K resides, has the largest effects on kinetics and steady-state inactivation^{30,33,35,36}. The charge reversal mutant, E1784K, is thought to disturb the integrity of CTD, causing the α_6 to become more mobile (Fig. 1)³⁷. A disturbance to α_6 integrity has been correlated with elevations in late I_{Na} and enhanced slow inactivation^{16,35,38–40}, which are key biophysical attributes in E1784K^{12,22,28}.

Recent studies characterized the effects of exercise-induced triggers on E1784K. These triggers include acidosis, elevated temperatures, and cytosolic calcium. Acidosis and elevated temperatures augment late I_{Na} and decrease peak I_{Na} in E1784K^{41–43}. Use-dependence in E1784K is reduced with high stimulation frequencies at elevated temperatures⁴¹. Compared to other mutants, E1784K tends to hamper the native potency of cytosolic calcium to block late I_{Na} in $Na_v1.5$ ^{37,44}. Elevated cytosolic calcium augments channel availability in E1784K by depolarizing the voltage-dependence of slow inactivation³⁷. Dynamic *in silico* action potential (AP) simulations in cardiac cells show E1784K-induced alternans at sinus rhythm and with tachycardia^{37,41}.

Department of Biomedical Physiology and Kinesiology, Simon Fraser University, 8888 University Drive, Burnaby, BC, V5A 1S6, Canada. Correspondence and requests for materials should be addressed to P.C.R. (email: pruben@sfu.ca)

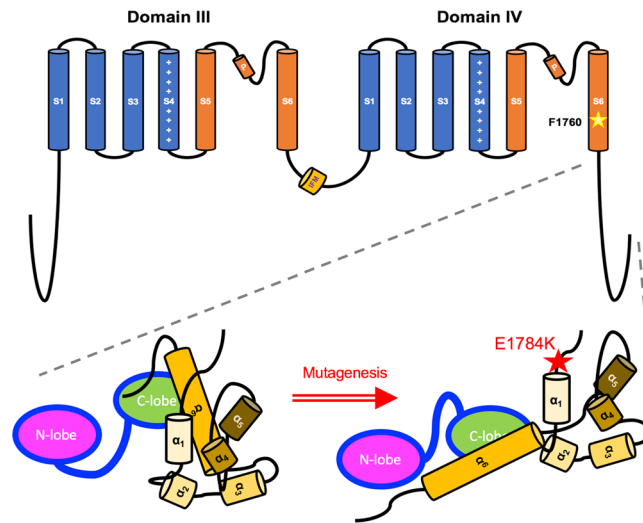


Figure 1. Sodium Channel Schematic Diagram. Domain III and Domain IV, along with their inter-linker and the CTD, regulate channel function and calcium sensitivity. DIII-DIV linker contains the fast inactivation “particle” (IFM motif). DIV-S6 contains the putative drug-binding residue, F1760, which is key for Ranolazine binding. The enlarged CTD contains six α -helices which aggregate to form an intact domain for calmodulin binding. Calmodulin (CaM) binds to the IQ-domain (α_6) under low cytosolic calcium conditions (structure adapted from Chagot *et al.*, 2009 and Gabelli *et al.*, 2014). E1784K may rearrange CTD structure affecting Calmodulin interaction with other channel sites, such as the DIII-DIV linker.

We hypothesize that Ranolazine, which preferentially blocks late I_{Na} , is suitable for ameliorating the thermal and calcium-induced defects in E1784K. Although prescribed as an anti-anginal drug for diastolic dysfunction treatment^{45–47}, Ranolazine has anti-arrhythmic efficacy proven to be useful in treating *SCN5a* inherited conditions^{48–51}. Ranolazine efficacy is enhanced with *SCN5a* mutations or channel triggers, such as acidosis, which augment late I_{Na} ^{48,49,52–54}. We predicted that the channel mutation-trigger interaction may alter drug efficacy. Our goal is to study the effects of Ranolazine on E1784K under conditions of elevated temperature and cytosolic calcium levels.

Results

Ranolazine binds to Nav1.5 inner vestibule. The $Na_v1.5$ homology model based on Na_vPas ($Na_v1.5$ - Na_vPas) is shown in Fig. 2. The side view of the channel shows the four domains and their putative voltage and pore-forming segments (including the p-helices, extracellular and intracellular linkers). Na_vPas shares about 32% sequence identity with $Na_v1.5$. The aligned sequences for DIII-DIV linker and CTD are shown in Fig. 2. Ranolazine was auto-docked against $Na_v1.5$ - Na_vPas using AutoDock4. The highest affinity (-7.7 kcal/mol) binding mode is enlarged in Fig. 2. The compound formed polar and Van der Waals interaction with various residues located in all four domains: S401, V405, C896, N927, F1418, S1458, L1462, N1463, I1466, F1760, V1764, I1768. The aromatic residue, F1760, is outlined in Fig. 2 as it is a key putative binding site for many anti-arrhythmics, local anesthetics, and anticonvulsants^{52,55}. F1760 orientation with respect to Ranolazine supports its critical role in drug binding.

Ranolazine does not affect conductance. Raw current traces in Fig. 3 show the effects of $0 \mu M$ and $100 \mu M$ Ranolazine on WT and E178K at $0 nM$ and $2500 nM$ cytosolic calcium (only $34^\circ C$ shown). E1784K reduced ($p < 0.0001$) the peak current and conductance density compared to WT. Elevated temperature ($34^\circ C$) increased ($p < 0.0001$) peak current and conductance density in WT but not in E1784K. Ranolazine had no effect ($p > 0.05$) on peak current or conductance density (Table 1 and Fig. 3B).

Figure 3A shows normalized conductance plotted against the test potential at $34^\circ C$. E1784K ($p < 0.0001$) and elevated temperature ($p = 0.0003$) depolarized the conductance midpoint ($GV-V_{1/2}$). The conductance slope ($GV-z$) was reduced ($p < 0.0001$) in E1784K compared to WT and increased ($p < 0.0001$) when temperature was elevated in both channel variants. The interaction between channel variant and temperature had no effect on $GV-V_{1/2}$ and $GV-z$. Normalized conductance was unchanged in all conditions with Ranolazine (Table 2).

E1784K availability is decreased in Ranolazine. Normalized current is plotted against membrane potential in Fig. 4. E1784K hyperpolarized ($p < 0.0001$) the SSFI midpoint ($SSFI-V_{1/2}$) compared to WT. Elevated temperature depolarized ($p < 0.0001$) $SSFI-V_{1/2}$ in both WT and E1784K. At $34^\circ C$ and $0 nM$ cytosolic calcium, $SSFI-V_{1/2}$ in E1784K was hyperpolarized ($p < 0.0001$) in $100 \mu M$ Ranolazine compared to WT (Fig. 4C and Table 2). This effect was not significant at $2500 nM$ cytosolic calcium. Analogous to the shifts on $GV-z$, $SSFI-z$ was decreased in E1784K and increased with elevated temperature ($p < 0.0001$). The slope was reduced in all conditions when Ranolazine was increased from $10 \mu M$ to $100 \mu M$ ($p < 0.05$, Table 2).

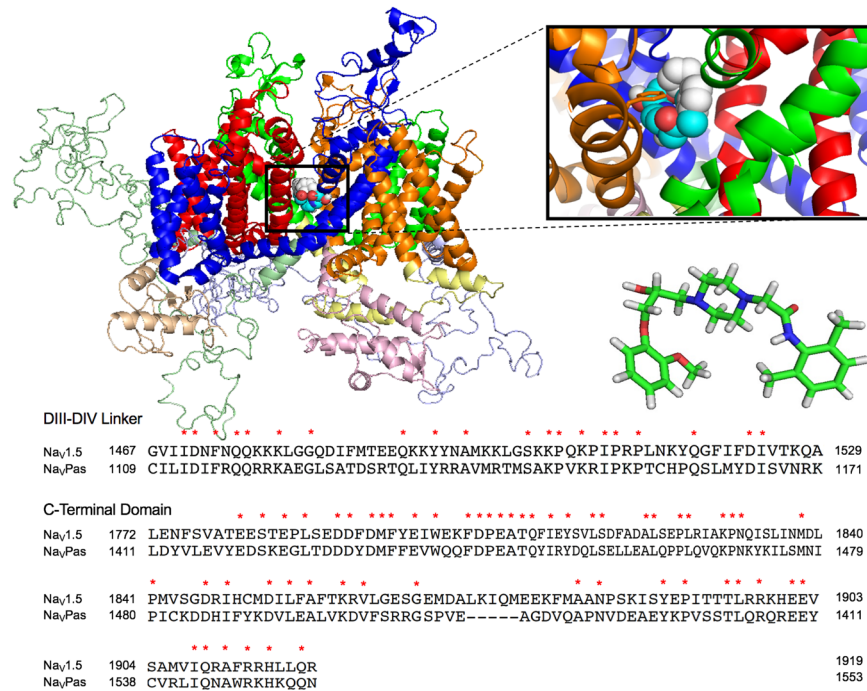


Figure 2. Ranolazine docked to Na_v.1.5-Na_v.Pas. The side view of Na_v.1.5-Na_v.Pas homology model is shown docked to Ranolazine. The enlarged inset shows the cartoon structure of the drug binding to the central domains of the channel. The aromatic F1760 residue is outlined. Below the inset is a 3D-structure of Ranolazine (Nitrogen is blue, Oxygen is red, Carbon is green, and Hydrogen is grey). Conserved residues in DIII-DIV linker and CTD between Na_v.1.5 and Na_v.Pas are indicated by a red asterisk.

Fast inactivation onset kinetics are not altered with Ranolazine. Fast inactivation onset kinetics at depolarized potentials (> -50 mV) were measured from τ_{on} of the mono-exponential fits. E1784K fast inactivation onset kinetics were accelerated regardless of temperature (Fig. 5A,B). Onset kinetics were accelerated (decreased τ_{on}) with elevated temperature in WT compared to E1784K ($p < 0.01$). WT and E1784K onset kinetics were decelerated (increased τ_{on} , $p < 0.05$) in Ranolazine as a function of voltage and cytosolic calcium at 22 °C (values reported in Table 3). These drug effects on τ_{on} were not significant at elevated temperature.

Figure 5C shows the Q_{10} values at 0 μ M and 10 μ M Ranolazine for all conditions. We observed high variability in the temperature coefficient at -50 mV compared to other voltages. At -50 mV, both Ranolazine and cytosolic calcium mutually affect thermosensitivity in WT: Q_{10} decreased at 0 nM cytosolic calcium and increased at 2500 nM cytosolic calcium in 10 μ M Ranolazine. At more depolarized voltages than -50 mV, subtle alterations occurred in Q_{10} (Fig. 5C). E1784K Q_{10} was not sensitive to Ranolazine. However, E1784K thermosensitivity was dampened in cytosolic calcium at -50 mV compared to other voltages and to WT.

Ranolazine does not suppress thermosensitive late I_{Na} in E1784K with elevated cytosolic calcium. Representative normalized late I_{Na} current traces are shown in Fig. 6A,B at 0 μ M and 100 μ M Ranolazine (only 34 °C shown). Late I_{Na} percent and density are shown in Fig. 6C,D as bar graphs. Late I_{Na} percent and density in E1784K increased ($p < 0.01$) by 11-fold and 7-fold, respectively, with elevated temperature at 0 nM cytosolic calcium (Fig. 6D and Table 4). This increase in late I_{Na} was almost fully attenuated in 10 μ M Ranolazine. Late I_{Na} percent decreased in elevated cytosolic calcium ($p < 0.01$) but there was no effect on late I_{Na} density in E1784K. Late I_{Na} percent and density in E1784K were not suppressed with Ranolazine at 2500 nM cytosolic calcium (Fig. 6D and Table 4).

Ranolazine does not enhance UDI in E1784K with elevated cytosolic calcium. Sustained or repetitive depolarizations induce slow inactivation in Na_v.1.5, which was indirectly measured by the use-dependent inactivation (UDI) protocols described in the methods. We were unable to measure fast inactivation recovery kinetics in E1784K which may be decelerated by Ranolazine and contribute to UDI⁵⁴. Use-dependence was measured at 1 Hz and 3 Hz, mimicking resting heart rate (60 bpm) and tachycardia (180 bpm), respectively. Normalized current plotted against time for UDI measured at 1 Hz and 3 Hz are shown in Fig. 7 (only 34 °C shown).

UDI plateau (y_0) was greater ($p = 0.0430$) at elevated temperature at both 1 Hz and 3 Hz, but the shift was larger in E1784K at 1 Hz (Table 5). y_0 decreased to different levels in Ranolazine (reported in Table 5). At high UDI frequencies, E1784K y_0 decreased in Ranolazine at 34 °C compared to WT (Fig. 7 shows only 34 °C, Table 5). Our statistical results suggest that the drug effects on UDI (3 Hz) in E1784K are limited in elevated cytosolic calcium (Table 5).

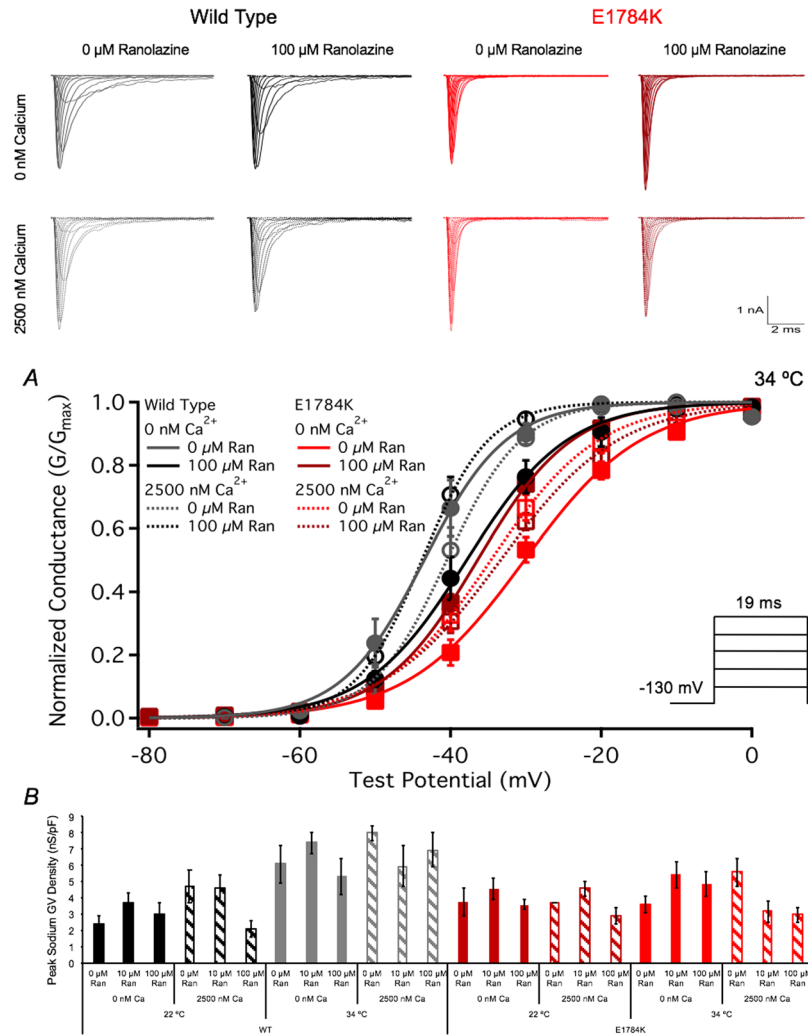


Figure 3. Ranolazine effects on channel conductance. Top traces show raw I_{Na} traces recorded at 34°C. Panel A shows normalized conductance plotted against the test potential (pulse protocol shown in *inset*) at 34°C. Panel C shows the peak conductance density bar graph versus all conditions at both 22°C and 34°C.

UDI onset kinetics were accelerated in E1784K and elevated temperature ($p < 0.05$), measured by τ_1 , at 1 Hz and 3 Hz. Onset kinetics decelerated in elevated cytosolic calcium ($p < 0.0001$) at 1 Hz predominately in WT compared to E1784K. WT and E1784K τ_1 was decreased ($p < 0.0001$) in Ranolazine at 2500 nM cytosolic calcium and 34°C (Table 5). τ_1 at 3 Hz was unaffected in Ranolazine. τ_2 was unaffected at 1 Hz and 3 Hz in all experimental conditions.

E1784K-induced alternans is exacerbated with Ranolazine. Biophysical data were extrapolated to physiological (37°C) and febrile (41°C) temperatures using a Q_{10} coefficient (Equation 6). Extrapolations were independently supported using Arrhenius relationships (Equation 7 and Table 6). Action potential (AP) traces are shown in Fig. 8 for simulations conducted in endocardial cells at three frequencies: 0.5 Hz (bradycardia), 1.5 Hz (sinus rhythm), and 2.5 Hz (tachycardia). At febrile temperature, simulated APs show accelerated depolarizations and repolarizations in WT compared to E1784K.

Electrical restitution curves (ERCs) at 90% repolarization were constructed from plotting APD_{90} against the diastolic interval as shown in Fig. 9A,B in endocardial cells. The last two beats were included in the ERCs to exemplify bifurcation and alternans-induction at critical diastolic intervals. The APD_{90} for WT follows a similar trend to previously published ERCs, typifying a relatively stable APD rate dependence^{56–58}. E1784K has a higher APD_{90} in all cardiac cells, especially the mid-myocardium, compared to WT (not shown in Fig. 9). At 37°C, the mutant causes bifurcation in APD_{90} , mainly in epicardial cells, indicative of alternans (not shown); however, endocardial cells also experience alternans at febrile temperature in addition to epicardial cells (Fig. 9B). Upon drug perfusion, bifurcations were observed at higher diastolic intervals in E1784K (Fig. 9). The drug-induced bifurcations in ERCs were augmented at febrile temperature in all cardiac cells.

A linear relationship is established between the last two AP beats at each frequency step (shown in Fig. 9C), with no alternans. Divergence from linearity is indicative of alternans occurrence. At both 37°C and 41°C, WT cells had no alternans, even upon 10 μ M Ranolazine perfusion, showing linearity with a slope = 1 (Fig. 9C). In

Condition	Peak I_{Na} Density (pA/pF)	N	Peak GV Density (nS/pF)	N
WT - 22 °C - 0 nM Ca^{2+} - 0 μ M Ran	148.97 \pm 35.10	7	2348.13 \pm 584.87	7
WT - 22 °C - 0 nM Ca^{2+} - 10 μ M Ran	241.31 \pm 41.80	5	3708.29 \pm 580.79	5
WT - 22 °C - 0 nM Ca^{2+} - 100 μ M Ran	184.16 \pm 40.16	5	3030.10 \pm 640.76	5
WT - 22 °C - 2500 nM Ca^{2+} - 0 μ M Ran	302.91 \pm 59.07	9	4714.99 \pm 971.64	9
WT - 22 °C - 2500 nM Ca^{2+} - 10 μ M Ran	250.88 \pm 45.34	7	4599.97 \pm 788.18	7
WT - 22 °C - 2500 nM Ca^{2+} - 100 μ M Ran	128.74 \pm 34.69	9	2088.79 \pm 517.47	9
WT - 34 °C - 0 nM Ca^{2+} - 0 μ M Ran	354.74 \pm 83.12	7	6067.75 \pm 1197.96	6
WT - 34 °C - 0 nM Ca^{2+} - 10 μ M Ran	472.24 \pm 55.47	5	7370.72 \pm 654.58	7
WT - 34 °C - 0 nM Ca^{2+} - 100 μ M Ran	369.56 \pm 81.13	8	5321.49 \pm 1074.25	8
WT - 34 °C - 2500 nM Ca^{2+} - 0 μ M Ran	535.63 \pm 70.44	6	7979.56 \pm 433.11	5
WT - 34 °C - 2500 nM Ca^{2+} - 10 μ M Ran	447.46 \pm 106.69	6	5948.51 \pm 1253.7	6
WT - 34 °C - 2500 nM Ca^{2+} - 100 μ M Ran	599.72 \pm 113.81	6	6935.36 \pm 1048.34	5
EK - 22 °C - 0 nM Ca^{2+} - 0 μ M Ran	214.56 \pm 50.18	7	3762.09 \pm 835.36	7
EK - 22 °C - 0 nM Ca^{2+} - 10 μ M Ran	265.65 \pm 51.36	8	4534.15 \pm 651.10	10
EK - 22 °C - 0 nM Ca^{2+} - 100 μ M Ran	240.86 \pm 24.43	7	3576.84 \pm 301.37	7
EK - 22 °C - 2500 nM Ca^{2+} - 0 μ M Ran	170.41 \pm 31.44	5	3660.43 \pm 1006.25	6
EK - 22 °C - 2500 nM Ca^{2+} - 10 μ M Ran	250.36 \pm 33.96	6	4562.87 \pm 453.93	8
EK - 22 °C - 2500 nM Ca^{2+} - 100 μ M Ran	183.02 \pm 44.18	5	2886.72 \pm 498.80	5
EK - 34 °C - 0 nM Ca^{2+} - 0 μ M Ran	257.99 \pm 34.07	8	3613.63 \pm 524.71	9
EK - 34 °C - 0 nM Ca^{2+} - 10 μ M Ran	322.26 \pm 47.45	6	5422.63 \pm 833.24	8
EK - 34 °C - 0 nM Ca^{2+} - 100 μ M Ran	278.25 \pm 67.75	8	4834.84 \pm 766.20	7
EK - 34 °C - 2500 nM Ca^{2+} - 0 μ M Ran	354.25 \pm 64.03	8	5587.74 \pm 831.96	7
EK - 34 °C - 2500 nM Ca^{2+} - 10 μ M Ran	227.98 \pm 41.82	5	3154.90 \pm 685.41	5
EK - 34 °C - 2500 nM Ca^{2+} - 100 μ M Ran	212.41 \pm 28.73	9	2959.51 \pm 471.73	9

Table 1. Peak I_{Na} Current and Conductance Density.

drug-free conditions, E1784K had a linear relationship at high BCLs (low frequencies), but deviated from linearity beginning at intermediate BCLs; distortion in linearity is observed at lower frequencies in epicardial cells (Fig. 9C). This relationship in E1784K is augmented with febrile temperature. The prolonged APD_{90} in E1784K were shortened with Ranolazine at very low frequencies, and alternans were quickly induced even during bradycardia, an effect exacerbated by febrile temperature (Fig. 9C).

Discussion

Our goal was to determine whether Ranolazine reduced channel dysfunction in E1784K under the triggering conditions of elevated temperature and cytosolic calcium. Ranolazine did not attenuate gain-of-function in E1784K when temperature and cytosolic calcium were elevated. Ranolazine has minimal effects on conductance in $Na_v1.5$ ^{48,49}. The drug follows the modulated receptor hypothesis, targeting the open/inactivated states at depolarized potentials, thereby suppressing late I_{Na} ⁵⁹. Physiological events, such as acidemia, enhance Ranolazine antiarrhythmic effect by augmenting late I_{Na} , thus providing the drug with a larger open-state channel substrate to target^{48,60,61}. In addition to physiological modulators, *SCN5a* mutations often alter voltage-dependence of the channel, which modify drug effects on $Na_v1.5$. To date, Ranolazine has been screened against only Δ KPQ^{50,52}, Y1767C⁴⁹, R1623Q⁵¹, and D1790G⁶². Our study is the first to show the combined external triggers and *SCN5a* mutation effects on Ranolazine.

Ranolazine efficacy was enhanced at elevated temperature. Similar to acidosis effects, elevated temperature increases the late open probability in E1784K^{48,53}. Late I_{Na} percent and density increased by 11- and 7-fold, respectively, with elevated temperature. We previously reported a 3.54-fold increase in late I_{Na} percent when temperature was elevated from 22 °C to 34 °C⁴¹; however, we used CHOK1 cells to study E1784K thermosensitivity. The temperature coefficient (Q_{10}) partly depends on lipid-channel interactions in the membrane, which differ between heterologous expression systems^{63,64}. The HEK293 lipid bilayer is less viscous than CHOK1 cells as observed in our whole-cell recordings, which may justify the heightened Q_{10} in the late I_{Na} measurements. At elevated stimulation frequencies and temperature, therapeutic Ranolazine decreased channel availability by increasing channel use-dependence in E1784K.

Although Ranolazine efficacy appears to be increased by temperature, its efficacy appears to be dampened by the combination of both elevated temperature and cytosolic calcium. At 34 °C, E1784K late I_{Na} percent was depressed with elevated cytosolic calcium, but there was no effect on late I_{Na} density. These opposing changes in late I_{Na} percent and density may be attributed to the increased peak I_{Na} density with elevated cytosolic calcium at 34 °C. Although not significant, the shift contributes to late I_{Na} percent calculation (Table 1). Late I_{Na} in E1784K was not attenuated by Ranolazine at elevated temperature and cytosolic calcium.

Drug Binding in Mutant-Trigger Context. Ranolazine action on $Na_v1.5$ is commonly associated with the modulated receptor hypothesis⁶⁵. Sokolov *et al.* argued that the drug follows a modified form of binding, as

Condition	GV- $V_{1/2}$ (mV)	GV-z	N	SSFI- $V_{1/2}$ (mV)	SSFI-z	N
WT - 22°C - 0 nM Ca^{2+} - 0 μ M Ran	-40.45 \pm 1.24	3.76 \pm 0.33	7	-88.62 \pm 1.99	-3.93 \pm 0.26	7
WT - 22°C - 0 nM Ca^{2+} - 10 μ M Ran	-45.59 \pm 1.09	5.37 \pm 0.29	6	-86.51 \pm 1.36	-3.95 \pm 0.16	7
WT - 22°C - 0 nM Ca^{2+} - 100 μ M Ran	-44.13 \pm 3.07	4.84 \pm 0.56	5	-88.45 \pm 3.18	-2.87 \pm 0.11 ^{*2}	6
WT - 22°C - 2500 nM Ca^{2+} - 0 μ M Ran	-42.22 \pm 1.16	4.08 \pm 0.25	9	-91.72 \pm 1.72	-3.68 \pm 0.15	9
WT - 22°C - 2500 nM Ca^{2+} - 10 μ M Ran	-44.40 \pm 2.22	3.87 \pm 0.28	7	-91.44 \pm 1.63	-3.93 \pm 0.18	7
WT - 22°C - 2500 nM Ca^{2+} - 100 μ M Ran	-44.76 \pm 2.09	4.38 \pm 0.36	9	-90.94 \pm 1.64	-2.20 \pm 0.13 ^{*2}	7
WT - 34°C - 0 nM Ca^{2+} - 0 μ M Ran	-43.44 \pm 2.06	6.00 \pm 0.45	6	-80.31 \pm 1.17	-4.72 \pm 0.18	6
WT - 34°C - 0 nM Ca^{2+} - 10 μ M Ran	-37.93 \pm 1.97	4.95 \pm 0.28	7	-82.51 \pm 2.26	-4.00 \pm 0.14	8
WT - 34°C - 0 nM Ca^{2+} - 100 μ M Ran	-37.58 \pm 2.03	4.43 \pm 0.33	7	-87.30 \pm 2.73	-2.82 \pm 0.16 ^{*2}	7
WT - 34°C - 2500 nM Ca^{2+} - 0 μ M Ran	-40.62 \pm 1.44	5.96 \pm 0.35	6	-80.25 \pm 2.30	-4.24 \pm 0.08	7
WT - 34°C - 2500 nM Ca^{2+} - 10 μ M Ran	-38.03 \pm 3.69	5.15 \pm 0.40	6	-83.18 \pm 3.95	-4.00 \pm 0.13	6
WT - 34°C - 2500 nM Ca^{2+} - 100 μ M Ran	-43.69 \pm 0.98	6.30 \pm 0.48	6	-90.43 \pm 2.80	-3.18 \pm 0.2 ^{*2}	6
EK - 22°C - 0 nM Ca^{2+} - 0 μ M Ran	-35.13 \pm 2.70	2.99 \pm 0.27	8	-100.46 \pm 1.51	-2.97 \pm 0.08	8
EK - 22°C - 0 nM Ca^{2+} - 10 μ M Ran	-35.83 \pm 1.65	3.14 \pm 0.27	10	-99.37 \pm 1.61	-2.88 \pm 0.08	10
EK - 22°C - 0 nM Ca^{2+} - 100 μ M Ran	-36.16 \pm 1.87	3.95 \pm 0.17	7	-103.83 \pm 2.42	-1.77 \pm 0.06 ^{*2}	8
EK - 22°C - 2500 nM Ca^{2+} - 0 μ M Ran	-39.33 \pm 2.02	3.09 \pm 0.16	5	-101.30 \pm 3.14	-3.07 \pm 0.21	6
EK - 22°C - 2500 nM Ca^{2+} - 10 μ M Ran	-34.88 \pm 1.57	2.83 \pm 0.15	8	-100.76 \pm 1.83	-3.11 \pm 0.13	8
EK - 22°C - 2500 nM Ca^{2+} - 100 μ M Ran	-33.72 \pm 1.52	3.02 \pm 0.35	5	-106.45 \pm 2.29	-2.12 \pm 0.08 ^{*2}	5
EK - 34°C - 0 nM Ca^{2+} - 0 μ M Ran	-30.22 \pm 1.27	3.68 \pm 0.28	9	-91.02 \pm 2.79	-3.18 \pm 0.14	9
EK - 34°C - 0 nM Ca^{2+} - 10 μ M Ran	-36.80 \pm 1.20	4.31 \pm 0.38	9	-94.20 \pm 3.73	-3.14 \pm 0.13	9
EK - 34°C - 0 nM Ca^{2+} - 100 μ M Ran	-35.53 \pm 1.18	4.11 \pm 0.22	8	-105.48 \pm 1.64 ^{*1}	-2.07 \pm 0.07 ^{*2}	8
EK - 34°C - 2500 nM Ca^{2+} - 0 μ M Ran	-34.74 \pm 1.48	4.06 \pm 0.41	8	-96.78 \pm 4.70	-3.26 \pm 0.12	8
EK - 34°C - 2500 nM Ca^{2+} - 10 μ M Ran	-31.25 \pm 2.04	3.92 \pm 0.35	7	-95.01 \pm 3.23	-2.94 \pm 0.15	7
EK - 34°C - 2500 nM Ca^{2+} - 100 μ M Ran	-32.33 \pm 1.64	3.39 \pm 0.15	9	-105.73 \pm 2.44	-2.00 \pm 0.06 ^{*2}	10

Table 2. Activation and Steady-State Fast Inactivation. ^{*1} $p < 0.01$ vs 0 μ M and 10 μ M Ran of same condition. ^{*2} $p < 0.05$ vs 0 μ M and 10 μ M Ran of same condition.

their pharmacological analysis suggested drug-binding at hyperpolarized voltages⁴⁸. Ranolazine exhibits partial preference to the closed state in $Na_v1.5$, as suggested by the hyperpolarizing shift in SSFI observed with Ranolazine. The shift mainly decreases channel availability near resting potential in cardiomyocytes. Other classic antiarrhythmics, anticonvulsants, and local anesthetics have similar effects, yet follow the modulated receptor hypothesis^{59,66}. Sokolov *et al.* also report that the drug-induced block in late I_{Na} occurs by a slow-mode recovery in slow inactivation, which is exacerbated at low pH⁴⁸. This effect was mildly observed in this study. However, it is difficult to correlate the drug effects in E1784K UDI to late I_{Na} , as the former had minor but significant shifts.

Ranolazine shares a very similar structure with the class 1b antiarrhythmic drug lidocaine, which, like other sodium blockers, preferentially binds to F1760 and, to a lesser extent, Y1767 in DIVS6^{49,52}. Ranolazine has high lipophilicity and can only bind to its receptor sites by traversing the phospholipid membrane and entering the central cavity through the inner vestibule. However, lateral pores, known as fenestrations, are alternative routes for large compounds like Ranolazine to access the central cavity. The fenestrations in the $Na_vPas-Na_v1.5$ model were unavailable for drug binding in auto-docking due to their constricted sizes⁶⁷. It would be interesting to determine whether E1784K alters fenestration size in $Na_v1.5$, modifying drug entry via the fenestrations.

The interaction between Ranolazine and extracellular channel regions is unknown, but is unlikely due to its lipophilicity; a crystal structure of the channel/drug interaction would elucidate the drug-induced modifications in gating. The newly discovered aryl sulfonamide antagonists preferentially stabilize $Na_v1.7$ DIVS4 activation thereby stabilizing the fast inactivated state and suppressing late I_{Na} ⁶⁸. Ranolazine may be structurally modified to include other moieties, like anionic aryl sulfonamides, for further optimizing its selectivity for targeting late versus peak I_{Na} .

E1784K-induced Structural Rearrangements in $Na_v1.5$ and its Impact on Ranolazine. We speculate E1784K affects fast inactivation via two possible mechanisms in $Na_v1.5$, thereby altering drug-channel interactions. Figure 1 shows the channel structures discussed, as follows:

- (1) E1784K hyperpolarizes the voltage-dependence of SSFI, thus stabilizing the interaction between the channel and the fast inactivation particle^{7,11,12,22,28}. Fast inactivation onset is correlated with DIVS4 activation, whereas channel recovery is rate limited by charge immobilization of DIVS4^{69,70}. The charge reversal mutant, E1784K, may enhance the transition of DIVS4 between closed and open states, as suggested by the Peters-Ruben model⁴³. We postulate that this effect may be due to an electrostatic repulsion between the CTD mutant and conserved positive residues in DIVS4, given their close proximity⁶⁷. This repulsion could make the DIVS4 in E1784K more mobile, which might explain the accelerated fast inactivation onset and recovery kinetics^{22,37,41,43}. Fast inactivation kinetics in E1784K are not enhanced by temperature, so it does not seem justified to attribute the thermosensitive late I_{Na} in E1784K to increased recovery kinetics. Rather a rearrangement may occur in DIVS4, conforming the voltage sensor to a state in which conductance in E1784K is higher⁴³.

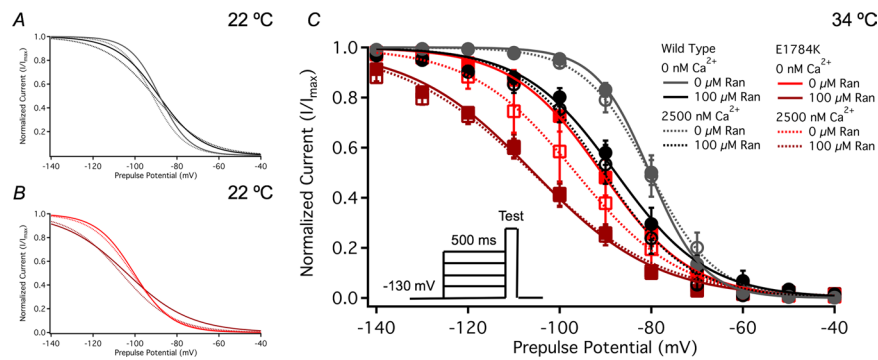


Figure 4. Ranolazine effects on steady-state fast inactivation. Panels A,B (22 °C) and C (34 °C) shows steady-state fast inactivation as normalized current plotted against the prepulse potential (pulse protocol shown in C inset).

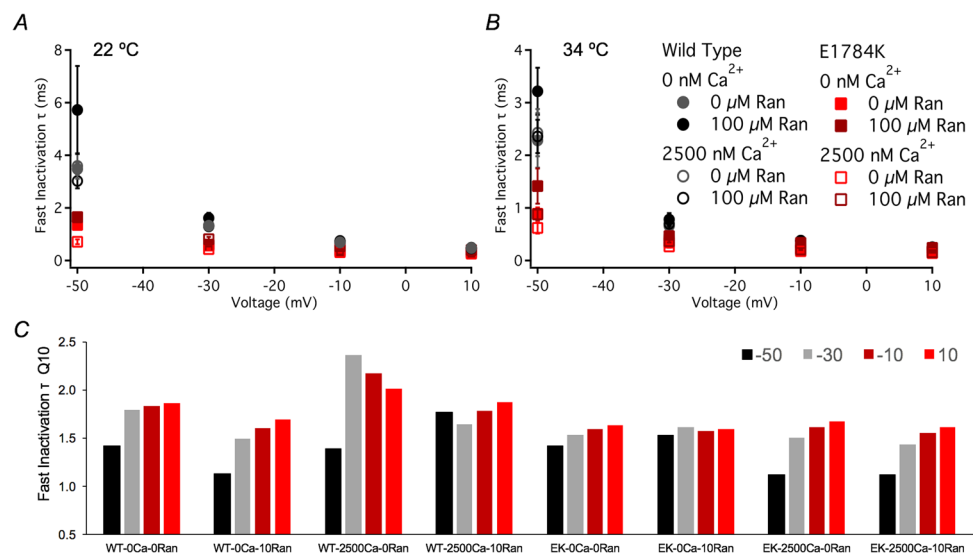


Figure 5. Ranolazine effects on fast inactivation onset time constants. Panels A,B show the single-exponential time constants plotted against voltage. The pulse protocol is identical to that used to measure channel conductance (refer to *Methods*). Panel C includes Q_{10} coefficient values for all conditions between -50 mV to $+10$ mV. Cytosolic calcium seems to modulate Ranolazine effects on WT Q_{10} , as elevated cytosolic calcium heightened thermosensitivity. Cytosolic calcium made -50 mV fast inactivation onset in E1784K less thermosensitive, consistent with decoupling between CTD and Domain III-IV linker mechanism, explained in the discussion.

- (2) E1784K alters the structure of CTD by disrupting the native hydrophobic and electrostatic interactions holding the EF-like hand domain (α_1 – α_4) tight with the IQ motif (α_6)³¹. Calcium sensitivity is imparted in $Na_v1.5$ via CaM, which binds to the IQ motif (α_6) via its C-lobe or N-lobe depending on cytosolic calcium levels^{71–73}. During diastole or systole, CaM is calcified to different extents at its N-lobe⁷⁴. Calcified CaM has a lower affinity for the IQ motif and binds, via its C-lobe, to DIII-DIV linker, forming a tripartite complex. This interaction is thought to prevent the DIII-DIV linker fast inactivation particle from occluding the pore, increasing channel availability near resting potential^{71,73}. With depolarized potentials, the CaM C-lobe stabilizes the fast inactivation particle, suppressing late I_{Na} , as in Δ KPQ and other mixed syndrome mutants^{37,40,44}. Some studies refute the tripartite complex formation and favor a $Ca_v1.2$ -like regulation of inactivation in $Na_v1.5$ ^{74,75}. In those studies, the calcium-calmodulin complex is localized to CTD^{76,77}. The Na_v Pas structure showed intermolecular interactions between DIII-DIV linker, CTD, and DIVS4⁶⁷. Motoike *et al.* reported CaM-independent interactions between the inter-linkers in $Na_v1.5$ ³⁶, suggesting that CaM acts as an auxiliary channel modifier during a calcium signal⁷⁵. Calcium regulation in $Na_v1.5$ is mediated by CaM since the dual EF-like hand domains in CTD do not bind calcium^{74,75}. In light of these structural models, we speculate that E1784K decouples both the calcium-dependent and calcium-independent interactions between the DIII-DIV linker and the CTD. Thus, E1784K inhibits calcium-dependent facilitation in $Na_v1.5$. We propose that the decoupling in CTD caused by E1784K may create a high entropy, unstable structure. Upon a calcium signal, the calcified calmodulin has reduced affinity for the IQ motif, thus augmenting CTD entropy⁷³.

Condition	-50 mV τ (ms)	-30 mV τ (ms)	-10 mV τ (ms)	+10 mV τ (ms)	N
WT - 22°C - 0 nM Ca ²⁺ - 0 μ M Ran	3.47 \pm 0.22	1.32 \pm 0.11	0.69 \pm 0.07	0.48 \pm 0.04	7
WT - 22°C - 0 nM Ca ²⁺ - 10 μ M Ran	3.28 \pm 0.45	1.13 \pm 0.06	0.61 \pm 0.04	0.44 \pm 0.03	5
WT - 22°C - 0 nM Ca ²⁺ - 100 μ M Ran	5.72 \pm 1.67 ^{*1}	1.61 \pm 0.20 ^{*2}	0.74 \pm 0.06	0.46 \pm 0.03	5
WT - 22°C - 2500 nM Ca ²⁺ - 0 μ M Ran	3.59 \pm 0.49	1.34 \pm 0.12	0.69 \pm 0.03	0.47 \pm 0.01	8
WT - 22°C - 2500 nM Ca ²⁺ - 10 μ M Ran	3.03 \pm 0.13	1.09 \pm 0.05	0.58 \pm 0.01	0.42 \pm 0.01	6
WT - 22°C - 2500 nM Ca ²⁺ - 100 μ M Ran	3.02 \pm 0.28	1.30 \pm 0.09	0.71 \pm 0.05	0.49 \pm 0.04	9
WT - 34°C - 0 nM Ca ²⁺ - 0 μ M Ran	2.28 \pm 0.52	0.66 \pm 0.07	0.34 \pm 0.02	0.23 \pm 0.01	5
WT - 34°C - 0 nM Ca ²⁺ - 10 μ M Ran	2.82 \pm 0.46	0.70 \pm 0.08	0.35 \pm 0.04	0.23 \pm 0.02	7
WT - 34°C - 0 nM Ca ²⁺ - 100 μ M Ran	3.22 \pm 0.45	0.78 \pm 0.12	0.38 \pm 0.06	0.22 \pm 0.02	5
WT - 34°C - 2500 nM Ca ²⁺ - 0 μ M Ran	2.43 \pm 0.45	0.48 \pm 0.04	0.27 \pm 0.01	0.20 \pm 0.01	6
WT - 34°C - 2500 nM Ca ²⁺ - 10 μ M Ran	1.53 \pm 0.24	0.60 \pm 0.10	0.29 \pm 0.03	0.20 \pm 0.02	4
WT - 34°C - 2500 nM Ca ²⁺ - 100 μ M Ran	2.36 \pm 0.32	0.69 \pm 0.08	0.38 \pm 0.04	0.25 \pm 0.02	6
EK - 22°C - 0 nM Ca ²⁺ - 0 μ M Ran	1.35 \pm 0.14	0.57 \pm 0.03	0.40 \pm 0.02	0.33 \pm 0.02	7
EK - 22°C - 0 nM Ca ²⁺ - 10 μ M Ran	1.46 \pm 0.17	0.54 \pm 0.03	0.36 \pm 0.02	0.30 \pm 0.02	10
EK - 22°C - 0 nM Ca ²⁺ - 100 μ M Ran	1.65 \pm 0.16	0.61 \pm 0.03	0.37 \pm 0.01	0.29 \pm 0.01	6
EK - 22°C - 2500 nM Ca ²⁺ - 0 μ M Ran	0.71 \pm 0.09	0.44 \pm 0.02	0.32 \pm 0.01	0.26 \pm 0.01	6
EK - 22°C - 2500 nM Ca ²⁺ - 10 μ M Ran	1.23 \pm 0.09	0.54 \pm 0.03	0.37 \pm 0.01	0.30 \pm 0.01	7
EK - 22°C - 2500 nM Ca ²⁺ - 100 μ M Ran	1.65 \pm 0.13	0.81 \pm 0.09	0.54 \pm 0.06 ^{*3}	0.40 \pm 0.03 ^{*4}	5
EK - 34°C - 0 nM Ca ²⁺ - 0 μ M Ran	0.89 \pm 0.12	0.34 \pm 0.02	0.23 \pm 0.02	0.18 \pm 0.01	9
EK - 34°C - 0 nM Ca ²⁺ - 10 μ M Ran	0.88 \pm 0.11	0.30 \pm 0.02	0.21 \pm 0.01	0.17 \pm 0.01	9
EK - 34°C - 0 nM Ca ²⁺ - 100 μ M Ran	1.41 \pm 0.34	0.47 \pm 0.09	0.34 \pm 0.07	0.24 \pm 0.05	8
EK - 34°C - 2500 nM Ca ²⁺ - 0 μ M Ran	0.62 \pm 0.11	0.27 \pm 0.02	0.18 \pm 0.01	0.14 \pm 0.01	9
EK - 34°C - 2500 nM Ca ²⁺ - 10 μ M Ran	1.08 \pm 0.07	0.35 \pm 0.05	0.22 \pm 0.02	0.17 \pm 0.01	6
EK - 34°C - 2500 nM Ca ²⁺ - 100 μ M Ran	0.88 \pm 0.11	0.37 \pm 0.02	0.21 \pm 0.01	0.16 \pm 0.01	8

Table 3. Open-State Fast Inactivation Time Constant. *¹p < 0.05 vs 0 μ M and 10 μ M Ran of same condition. *²p < 0.05 vs 10 μ M Ran of same condition. *³p < 0.01 vs 0 μ M Ran of same condition. *⁴p < 0.05 vs 0 μ M Ran of same condition.

Both mechanisms (1) and (2) may occur simultaneously in E1784K. The calcium effects in Na_v1.5 are localized to CTD. No reports have shown direct interaction between calcium-calmodulin and DIVS4, so if mechanism (2) occurs, it may be via an indirect effect on DIVS4.

In light of the discussed structural insights, we speculate that Ranolazine can easily access the inner vestibule with non-calcified calmodulin, since the molecule binds tightly to the IQ motif. Ranolazine efficacy, however, is hampered by cytosolic calcium, suggesting an interaction between the drug and the channel at CTD. The high entropy CTD in calcified calmodulin seems to physically hinder Ranolazine from entering into the inner vestibule.

Physiological and Medical Implications. Elevated temperature and cytosolic calcium are two of many other physiological triggers that occur during exercise and are common to other pathophysiological states, such as myocardial ischemia or infarction, and heart failure^{78,79}. The majority patients with *SCN5a* mutations show ameliorated LQT3 phenotype during exercise⁸⁰. Functional studies have correlated this to a stimulation frequency or calcium-induced reduction in late I_{Na}⁴⁴. However, it is clear from our study, focusing on E1784K, that the *SCN5a* mutant response to triggers can be unique^{37,41}. Thus, it is necessary to study antiarrhythmics in *SCN5a* cohorts during different physiological states as the mutant-trigger effect may determine drug efficacy.

Our AP simulations clearly show pro-arrhythmic effects of Ranolazine, which are exacerbated by febrile temperatures. Electrical restitution curves clearly show a critical diastolic interval at which alternans are triggered. Our AP simulations provide evidence of Ranolazine's arrhythmogenicity, as it does not shorten APD₉₀ in E1784K at high heart rates. At low heart rates and at body core temperature, the drug shortens APD₉₀ in cardiac cells. However, with normal and elevated heart rates, the drug induces alternans, an effect exacerbated at febrile temperature. The critical diastolic intervals at which alternans are caused by the drug appear earlier (at higher BCLs) at febrile temperature.

E1784K induces alternans with higher prevalence in epicardial cells at low heart rates. This result coincides with the phase 2 re-entry phenomenon constituting the repolarization hypothesis in BrS1⁷⁸. The high I_{Kto} density, especially in the right epicardium, results in complete action potential failure⁸¹. E1784K channels are less available for activation due to the hyperpolarized SSFI-V_{1/2}. This seems to be the main mechanism behind the decrease in AP upstroke velocity in cardiac cells, especially the epicardial cells, despite the mutant and triggers-exacerbated increased late I_{Na}. Thus, E1784K expresses both gain- and loss-of-function at the electrical level in cardiac cells. However, this expressivity is finely tuned by channel switches, like temperature and cytosolic calcium.

Our previous and current data suggest exercise, and its accompanying physiological triggers, differentially affect mixed syndrome mutations, especially E1784K^{22,37,41,42}. The action of different antiarrhythmics appear to differ depending on physiological state.

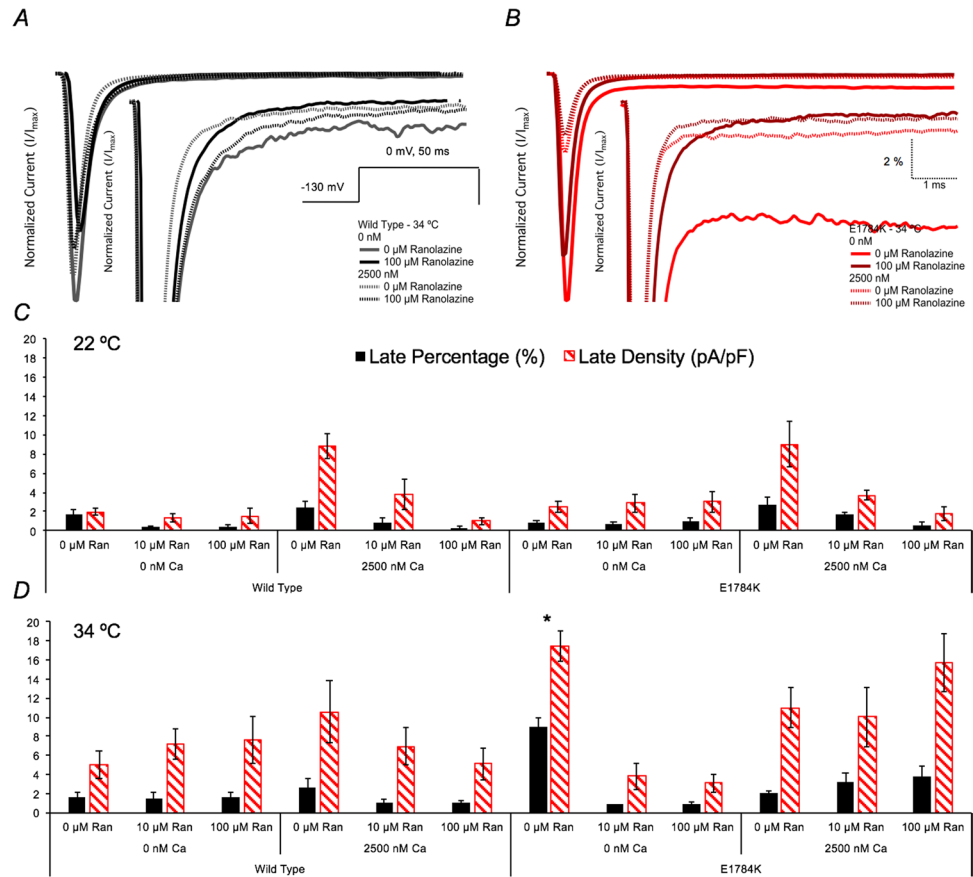


Figure 6. Ranolazine effects on late I_{Na} . Panels A,B show normalized current traces, with emphasis on the non-inactivating, late I_{Na} , at 34 °C. The normalized late I_{Na} in E1784K is enhanced drastically by elevated temperature. Cytosolic calcium suppresses the E1784K normalized late I_{Na} (addressed in discussions). Ranolazine suppresses late I_{Na} only at 0 nM compared to 2500 nM cytosolic calcium. Panels C,D show the late I_{Na} percent and density bar graphs for all conditions at 22 °C and 34 °C, respectively.

Conclusions

Appropriate management of cardiac arrhythmias in *SCN5a* patients requires careful investigation of antiarrhythmic drug efficacy under various physiological states. Our results suggest that Ranolazine may increase the susceptibility for arrhythmia development in E1784K carriers at sinus rhythm and tachycardia. The risk is augmented under febrile conditions. Although exercise is commonly associated with high heart rates, other pathophysiological states share common triggers, as in heart failure or myocardial ischemia and infarction. Other antiarrhythmics should also be screened against E1784K and other channel mutants under various physiological conditions.

Methods

Homology Modelling and Auto-Docking. Homology modeling was performed using the Swiss-Model server (<https://swissmodel.expasy.org>)⁸². The newly cryo-EM solved American cockroach voltage-gated sodium channel (Na_V Pas) structure (3.8-Å resolution) was used as a template against the Na_V 1.5 sequence. Modeling was done according to the protocol established by Bordoli *et al.*⁸². Sequence alignment was performed using Uniprot Align (<http://www.uniprot.org/align/>) for SCN5A_HUMAN (Na_V 1.5) and SCNA1_PERAM (Na_V Pas).

Ranolazine was virtually docked using AutoDock4 against the Na_V 1.5 homology model built on Na_V Pas (Na_V 1.5- Na_V Pas)⁸³. PyMOL-pdb viewer was used for optimization and visualization of the auto-docking results.

Ethical approval. The research was approved by Biohazards review 251–2012 issued by the office of the Environmental Health and Safety at Simon Fraser University, Burnaby, BC, Canada.

Cell Culture. HEK293 cells were grown at pH 7.4 in a DMEM (1x) nutrient medium (Life Technologies, NY, USA), supplemented with 10% FBS and maintained in a humidified environment at 37 °C with 5% CO_2 . The α subunits (WT or E1784K) were co-transfected with the β 1 subunit and green fluorescent protein, eGFP (1.50 μ g: 0.75 μ g: 1.50 μ g, respectively). The cDNA mixture was then allowed to incubate with the HEK293 cells before plating on coverslips. The HEK293 cells were selected for this study since they contain a relatively elevated $[CaM]_{free}$ level compared to other cell lines, thereby controlling for calcium-calmodulin effects on Na_V 1.5⁸⁴.

Condition	Late I_{Na} Density (pA/pF)	N	Late Percent (%)	N
WT - 22 °C - 0 nM Ca^{2+} - 0 μ M Ran	1.95 \pm 0.34	9	1.71 \pm 0.54	9
WT - 22 °C - 0 nM Ca^{2+} - 10 μ M Ran	1.35 \pm 0.44	8	0.35 \pm 0.12	8
WT - 22 °C - 0 nM Ca^{2+} - 100 μ M Ran	1.55 \pm 0.79	6	0.45 \pm 0.20	6
WT - 22 °C - 2500 nM Ca^{2+} - 0 μ M Ran	8.83 \pm 1.33	8	2.41 \pm 0.72	6
WT - 22 °C - 2500 nM Ca^{2+} - 10 μ M Ran	3.78 \pm 1.64	8	0.80 \pm 0.48	7
WT - 22 °C - 2500 nM Ca^{2+} - 100 μ M Ran	1.01 \pm 0.38	7	0.30 \pm 0.12	6
WT - 34 °C - 0 nM Ca^{2+} - 0 μ M Ran	5.04 \pm 1.42	7	1.57 \pm 0.52	9
WT - 34 °C - 0 nM Ca^{2+} - 10 μ M Ran	7.21 \pm 1.61	8	1.54 \pm 0.54	8
WT - 34 °C - 0 nM Ca^{2+} - 100 μ M Ran	7.66 \pm 2.47	9	1.67 \pm 0.42	9
WT - 34 °C - 2500 nM Ca^{2+} - 0 μ M Ran	10.57 \pm 3.2	7	2.71 \pm 0.90	9
WT - 34 °C - 2500 nM Ca^{2+} - 10 μ M Ran	6.95 \pm 1.97	8	1.09 \pm 0.26	8
WT - 34 °C - 2500 nM Ca^{2+} - 100 μ M Ran	5.11 \pm 1.67	4	0.98 \pm 0.25	5
EK - 22 °C - 0 nM Ca^{2+} - 0 μ M Ran	2.51 \pm 0.63	9	0.85 \pm 0.20	9
EK - 22 °C - 0 nM Ca^{2+} - 10 μ M Ran	2.86 \pm 0.88	9	0.68 \pm 0.21	8
EK - 22 °C - 0 nM Ca^{2+} - 100 μ M Ran	3.01 \pm 1.08	10	1.02 \pm 0.39	8
EK - 22 °C - 2500 nM Ca^{2+} - 0 μ M Ran	9.02 \pm 2.31	5	2.64 \pm 0.81	4
EK - 22 °C - 2500 nM Ca^{2+} - 10 μ M Ran	3.68 \pm 0.51	9	1.65 \pm 0.30	9
EK - 22 °C - 2500 nM Ca^{2+} - 100 μ M Ran	1.78 \pm 0.65	8	0.61 \pm 0.30	6
EK - 34 °C - 0 nM Ca^{2+} - 0 μ M Ran	17.47 \pm 1.54 ^{*1}	6	8.97 \pm 1.02 ^{*1}	6
EK - 34 °C - 0 nM Ca^{2+} - 10 μ M Ran	3.84 \pm 1.39	4	0.86 \pm 0.04	4
EK - 34 °C - 0 nM Ca^{2+} - 100 μ M Ran	3.09 \pm 0.96	6	0.89 \pm 0.22	6
EK - 34 °C - 2500 nM Ca^{2+} - 0 μ M Ran	11.01 \pm 2.12	7	2.00 \pm 0.34	9
EK - 34 °C - 2500 nM Ca^{2+} - 10 μ M Ran	10.05 \pm 3.08	5	3.28 \pm 0.93	6
EK - 34 °C - 2500 nM Ca^{2+} - 100 μ M Ran	15.73 \pm 6.24	5	3.76 \pm 1.10	4

Table 4. Late I_{Na} Current Density and Percentage. ^{*1} $p < 0.01$ vs 10 μ M and 100 μ M Ran of same condition.

Electrophysiology. Whole-cell patch clamp recordings were performed in extracellular solution containing (mM): 96 NaCl, 4 KCl, 2 $CaCl_2$, 1 $MgCl_2$, and 10 HEPES (pH 7.4). Solutions were titrated with CsOH to pH 7.4. Pipettes were fabricated with a P-1000 puller using borosilicate glass (Sutter Instruments, CA, USA), dipped in dental wax to reduce capacitance, then thermally polished to a resistance of 1.0–1.5 M Ω . Low resistance electrodes were used to minimize series resistance between pipette and intracellular solution resulting in typical access resistances of 3.5 M Ω or less, thereby minimizing voltage measurement error. Pipettes were filled with intracellular solution. For minimal cytosolic calcium levels, pipettes contained (mM): 130 CsF, 9.6 NaCl, 10 HEPES, and 10 EGTA titrated to pH 7.4. The intracellular pipette solution was manipulated to mimic peak systolic cytosolic calcium^{85,86}. To do so, we calculated, using the Ca-EGTA Calculator v1.3, the amount of $CaCl_2$ (in mM) added to bring cytosolic calcium to 2500 nM at both 22 °C and 34 °C: 9.53 and 9.60, respectively.

All recordings were made using an EPC-9 patch-clamp amplifier (HEKA Elektronik, Lambrecht, Germany) digitized at 20 kHz using an ITC-16 interface (HEKA Elektronik, Lambrecht, Germany). Data were acquired and low-pass-filtered (5 kHz) using PatchMaster/FitMaster software (HEKA Elektronik, Lambrecht, Germany) running on an Apple iMac (Apple Computer, Cupertino, CA). Leak subtraction was performed online using a P/4 procedure. Bath solution temperature was controlled using a Peltier device driven by a TC-10 Temperature Controller (Dagan, Minneapolis, MN). Bath temperature was maintained at 22 °C or 34 °C. Experiments were not performed at physiological temperatures because of the inherent instability of cells at temperatures above 34 °C. We extrapolated data to physiological temperatures using a Q_{10} relationship, which was supported with Arrhenius calculations, (described below). After a giga ohm seal resistance was achieved, the whole-cell configuration was attained. The holding potential between protocols was -110 mV. We recorded I_{Na} from cells that expressed currents no greater than -5 nA. The average voltage error calculated for all cells used in this study ($n = 250$) is 6.06 mV \pm 0.40 mV obtained (Table 7). There are no differences between the voltage-errors in the different conditions ($p > 0.05$).

Drug Preparation. Ranolazine was obtained from Gilead Sciences (Foster City, CA) in powder form, diluted to 100 mM stock in 0.1 M HCl, aliquoted at 10 mM and stored at -20 °C. Working concentrations of 10 μ M (therapeutic concentration) or 100 μ M (non-therapeutic) were freshly prepared in bath solution. pH was readjusted before performing electrophysiological experiments. Due to the large number of experimental conditions and the challenges of maintaining whole-cell recordings at elevated temperature, we performed unmatched pair experiments.

Analysis and Statistics. Analysis and graphing were done using FitMaster software (HEKA Elektronik, Lambrecht, Germany) and Igor Pro (Wavemetrics, Lake Oswego, OR, USA) with statistical information derived using JMP statistical software. Statistical significance was accepted at $p < 0.05$ using a four-factor completely randomized design (CRD) ANOVA test followed by a post-hoc Tukey test. Our statistical model was a full factorial in

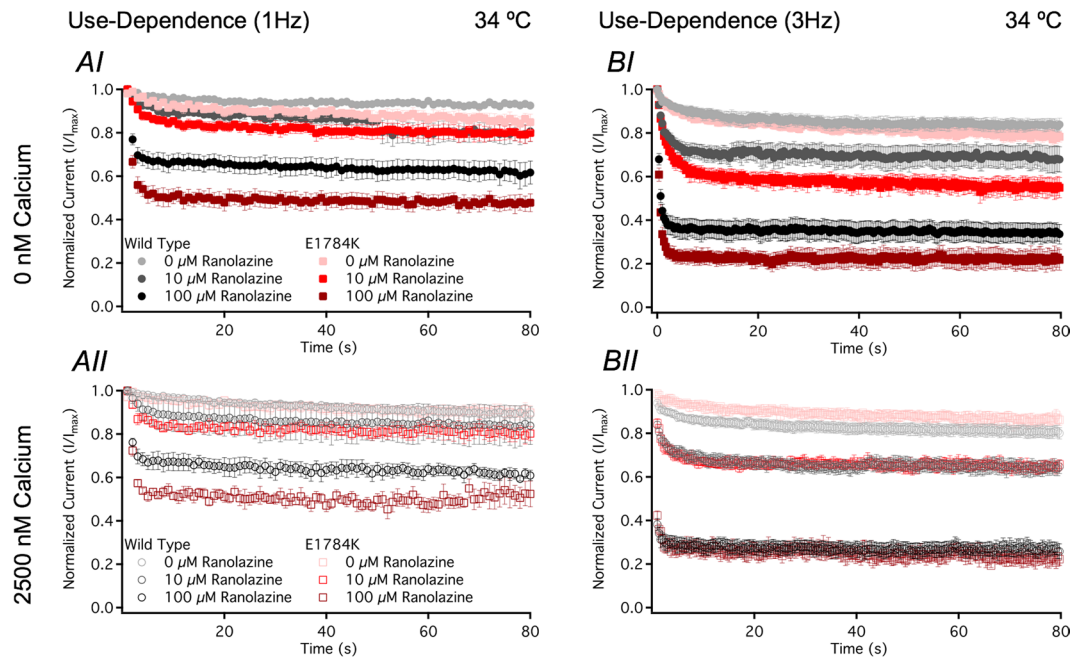


Figure 7. Ranolazine effects on use-dependence. Panels AI-II and Panels BI-II show normalized current versus time measuring UDI at 1 Hz and 3 Hz, respectively. Insets are excluded for visual clarity (refer to methods for pulse protocols). All three drug concentrations are included in the figures to show 10 μM Ranolazine effect on UDI (3 Hz) in E1784K at 0 nM compared to 2500 nM.

which all the factors were allowed to interact together yielding multiple effect tests: Ranolazine, Channel Variant, Ranolazine \times Channel Variant, Temperature, Ranolazine \times Temperature, Channel Variant \times Temperature, Ranolazine \times Channel Variant \times Temperature, Calcium, Ranolazine \times Calcium, Channel Variant \times Calcium, Ranolazine \times Channel Variant \times Calcium, Temperature \times Calcium, Ranolazine \times Temperature \times Calcium, Channel Variant \times Temperature \times Calcium, Ranolazine \times Channel Variant \times Temperature \times Calcium. All values reported in the results sections are given as means \pm standard error of means.

Voltage Protocols. *Current Density.* We measured current density from the ratio of current amplitude to the cell membrane capacitance (pA/pF).

Conductance Density. Channel conductance was calculated from peak I_{Na} using Ohm's law at 0 mV.

$$G_{\text{Na}} = I_{\text{Na}}/V - E_{\text{rev}} \quad (1)$$

where G_{Na} is sodium channel conductance, I_{Na} is peak sodium current in response to the command potential $V = 0$ mV, and E_{rev} is the reversal potential. We measured conductance density from the ratio of conductance to the cell membrane capacitance (nS/pF).

Activation (GV). To determine the voltage dependence of activation, we measured the peak current amplitude at test pulse potentials ranging from -100 mV to $+80$ mV in increments of $+10$ mV for 19 ms. Prior to the test pulse, channels were allowed to recover from fast inactivation at -130 mV for 197 ms. Channel conductance was calculated from peak I_{Na} using Formula (1). Calculated values for conductance were normalized to the maximal conductance and fit with the Boltzmann function:

$$G/G_{\text{max}} = 1/(1 + \exp[-ze_0[V_m - V_{1/2}]/kT]) \quad (2)$$

where G/G_{max} is the normalized conductance amplitude, V_m is the command potential, z is the apparent valence, e_0 is the elementary charge, $V_{1/2}$ is the midpoint voltage, k is the Boltzmann constant, and T is temperature in $^{\circ}\text{K}$.

Steady-State Fast Inactivation (SSFI). The voltage-dependence of SSFI was measured by preconditioning the channels to a hyperpolarizing potential of -130 mV and then eliciting prepulses from -130 or -150 to $+10$ mV in increments of 10 mV for 500 ms. Channel availability was assessed during a test pulse to 0 mV. Normalized current amplitude as a function of voltage was fit using the Boltzmann function:

$$I/I_{\text{max}} = 1/(1 + \exp(-ze_0(V_M - V_{1/2})/kT)) \quad (3)$$

where I/I_{max} is the normalized current amplitude, z is apparent valence, e_0 is the elementary charge, V_m is the prepulse potential, $V_{1/2}$ is the midpoint voltage of SSFI, k is the Boltzmann constant, and T is temperature in $^{\circ}\text{K}$.

Condition	1 Hz-y0	1 Hz-τ1 (s)	1 Hz-τ2 (s)	N	3 Hz-y0	3 Hz-τ1 (s)	3 Hz-τ2 (s)	N
WT - 22°C - 0 nM Ca ²⁺ - 0 μM Ran	0.84 ± 0.03	3.13 ± 0.88	47.88 ± 9.44	6	0.63 ± 0.04	2.03 ± 0.41	40.53 ± 5.42	7
WT - 22°C - 0 nM Ca ²⁺ - 10 μM Ran	0.77 ± 0.01	2.96 ± 0.52	18.55 ± 4.50	7	0.52 ± 0.02	3.39 ± 0.62	23.00 ± 7.54	7
WT - 22°C - 0 nM Ca ²⁺ - 100 μM Ran	0.44 ± 0.02 ^{*1}	2.19 ± 0.44	9.70 ± 3.31	5	0.15 ± 0.02 ^{*1}	0.92 ± 0.18	7.02 ± 4.44	4
WT - 22°C - 2500 nM Ca ²⁺ - 0 μM Ran	0.81 ± 0.02	8.22 ± 2.84	114.32 ± 22.42	7	0.66 ± 0.03	1.83 ± 0.23	36.4 ± 7.98	7
WT - 22°C - 2500 nM Ca ²⁺ - 10 μM Ran	0.78 ± 0.01	6.93 ± 0.94	31.93 ± 10.85	6	0.52 ± 0.02	1.19 ± 0.19	8.57 ± 0.42	5
WT - 22°C - 2500 nM Ca ²⁺ - 100 μM Ran	0.35 ± 0.03 ^{*1}	1.67 ± 0.12	34.32 ± 22.87	7	0.20 ± 0.03 ^{*1}	0.69 ± 0.32	14.56 ± 13.09	3
WT - 34°C - 0 nM Ca ²⁺ - 0 μM Ran	0.92 ± 0.01	4.77 ± 3.14	39.42 ± 20.36	4	0.84 ± 0.03	2.75 ± 1.00	17.73 ± 9.63	5
WT - 34°C - 0 nM Ca ²⁺ - 10 μM Ran	0.76 ± 0.05	5.41 ± 3.35	62.60 ± 20.25	5	0.65 ± 0.06	0.98 ± 0.10	16.65 ± 6.29	6
WT - 34°C - 0 nM Ca ²⁺ - 100 μM Ran	0.60 ± 0.06 ^{*2}	0.66 ± 0.10	43.51 ± 18.93	8	0.33 ± 0.05 ^{*1}	0.39 ± 0.08	13.99 ± 8.03	8
WT - 34°C - 2500 nM Ca ²⁺ - 0 μM Ran	0.88 ± 0.03	30.10 ± 6.41 ^{*3}	59.96 ± 37.08	4	0.79 ± 0.04	1.46 ± 0.17	38.85 ± 12.19	8
WT - 34°C - 2500 nM Ca ²⁺ - 10 μM Ran	0.82 ± 0.04	2.83 ± 1.02	67.05 ± 23.05	5	0.60 ± 0.03 ^{*4}	1.02 ± 0.16	17.28 ± 6.89	7
WT - 34°C - 2500 nM Ca ²⁺ - 100 μM Ran	0.64 ± 0.02	0.44 ± 0.16	8.44 ± 2.77	5	0.27 ± 0.03 ^{*1}	0.41 ± 0.06	17.80 ± 9.98	5
EK - 22°C - 0 nM Ca ²⁺ - 0 μM Ran	0.69 ± 0.06	3.37 ± 0.64	69.20 ± 25.09	6	0.79 ± 0.01	3.08 ± 1.61	32.65 ± 20.62	4
EK - 22°C - 0 nM Ca ²⁺ - 10 μM Ran	0.57 ± 0.05	3.25 ± 0.63	64.71 ± 37.46	7	0.47 ± 0.02 ^{*4}	2.40 ± 0.37	16.28 ± 3.57	6
EK - 22°C - 0 nM Ca ²⁺ - 100 μM Ran	0.27 ± 0.05 ^{*1}	1.87 ± 0.25	74.43 ± 28.56	8	0.14 ± 0.03 ^{*1}	1.00 ± 0.34	1.29 ± 0.19	4
EK - 22°C - 2500 nM Ca ²⁺ - 0 μM Ran	0.73 ± 0.02	1.99 ± 1.02	31.37 ± 6.74	4	0.69 ± 0.06	3.59 ± 1.84	8.20 ± 3.73	4
EK - 22°C - 2500 nM Ca ²⁺ - 10 μM Ran	0.59 ± 0.06	7.17 ± 1.35	75.52 ± 20.26	5	0.47 ± 0.04	3.38 ± 0.43	13.21 ± 1.51	5
EK - 22°C - 2500 nM Ca ²⁺ - 100 μM Ran	0.24 ± 0.04 ^{*1}	2.68 ± 1.13	70.86 ± 29.29	3	0.20 ± 0.06 ^{*2}	0.82 ± 0.29	1.94 ± 0.31	3
EK - 34°C - 0 nM Ca ²⁺ - 0 μM Ran	0.82 ± 0.04	6.76 ± 1.43	68.66 ± 25.39	8	0.77 ± 0.03	2.66 ± 0.45	49.11 ± 13.27	9
EK - 34°C - 0 nM Ca ²⁺ - 10 μM Ran	0.77 ± 0.06	2.40 ± 0.55	78.22 ± 35.32	7	0.55 ± 0.03 ^{*4}	1.63 ± 0.32	27.16 ± 15.43	5
EK - 34°C - 0 nM Ca ²⁺ - 100 μM Ran	0.47 ± 0.04 ^{*1}	0.77 ± 0.07	19.07 ± 9.49	6	0.21 ± 0.05 ^{*1}	0.40 ± 0.04	24.08 ± 18.78	5
EK - 34°C - 2500 nM Ca ²⁺ - 0 μM Ran	0.87 ± 0.03	15.05 ± 3.35 ^{*3}	65.60 ± 19.19	5	0.74 ± 0.08	2.50 ± 0.65	30.82 ± 2.43	6
EK - 34°C - 2500 nM Ca ²⁺ - 10 μM Ran	0.77 ± 0.04	1.77 ± 0.48	48.78 ± 22.76	5	0.63 ± 0.03	1.13 ± 0.12	6.41 ± 3.13	6
EK - 34°C - 2500 nM Ca ²⁺ - 100 μM Ran	0.46 ± 0.05 ^{*1}	1.21 ± 0.20	38.24 ± 19.24	5	0.26 ± 0.03 ^{*1}	0.54 ± 0.14	6.89 ± 4.62	5

Table 5. Use-Dependence (1 Hz and 3 Hz). ^{*1}p < 0.0001 vs 0 μM and 10 μM Ran of same condition. ^{*2}p < 0.0001 vs 0 μM Ran of same condition. ^{*3}p < 0.0001 vs 10 μM and 100 μM Ran of same condition. ^{*4}p < 0.0001 vs 0 μM and 100 μM Ran of same condition.

Fast Inactivation Onset. Time constants for open-state fast inactivation were derived by fitting a single exponential function to the decay of current obtained from the activation protocol.

$$I = I_{ss} + \alpha \exp(-(t - t_0)/\tau) \quad (4)$$

where I is current amplitude, I_{ss} is the plateau amplitude, α is the amplitude at time 0 for time constant τ, and t is time.

Late I_{Na} Current. Late I_{Na} was measured between 40–50 ms during a 50 ms depolarizing pulse to 0 mV from a holding potential of −130 mV. An average of 10 pulses was used to increase the signal-to-noise ratio.

Use-Dependent Inactivation (UDI, 1 Hz and 3 Hz). Channels accumulated into a use-dependent inactivated state during either a series of 300 380 ms depolarizing pulses to 0 mV followed by a 615 ms–110 mV recovery pulse at a frequency 1 Hz, or 500 220 ms depolarizing pulses to 0 mV followed by a 110 ms–110 mV recovery pulse at a frequency 3 Hz. Normalized current amplitude as a function of time was fit with a double exponential.

$$I = I_{ss} + \alpha_1 \exp(-t/\tau_1) + \alpha_2 \exp(-t/\tau_2) \quad (5)$$

where I is current amplitude, I_{ss} is the plateau amplitude, α₁ and α₂ are the amplitudes at time 0 for time constants τ₁ and τ₂, and t is time.

Q₁₀ Coefficients. The temperature coefficient for kinetic and thermodynamic parameters plotted as a function temperature was calculated in Igor:

$$Q_{10} = (R_2/R_1)^{10/(T_2-T_1)} \quad (6)$$

where R is the rate and T is temperature (1 and 2 are the two temperatures measured). Rate was calculated by the inverse of the τ value. Q₁₀ fits for steady-state midpoints and slopes were calculated by replacing the R_X with V_{1/2} and z values. Fits for y₀ were calculated based of the 1/y₀ to yield optimal Q₁₀ values. The fit was extrapolated to physiological (37 °C) and febrile (41 °C) temperatures.

Arrhenius Calculations. The Arrhenius linear relationship for the natural exponent of kinetic or thermodynamic parameters as a function of inverse temperature was calculated in Igor:

Condition	37°C (Q ₁₀)	41°C (Q ₁₀)	37°C (Arrhenius)	41°C (Arrhenius)
Peak GV Density (nS/pF)				
WT - 0 nM Ca ²⁺ - 0 μM Ran	16179.18	55592.62	8124.68	10881.05
WT - 0 nM Ca ²⁺ - 10 μM Ran	22678.58	99329.99	9107.70	11251.36
WT - 2500 nM Ca ²⁺ - 0 μM Ran	27586.50	131656.89	9377.01	11024.82
WT - 2500 nM Ca ²⁺ - 10 μM Ran	15043.82	48489.81	6439.00	6969.03
EK - 0 nM Ca ²⁺ - 0 μM Ran	3575.20	3527.30	3569.09	3525.15
EK - 0 nM Ca ²⁺ - 10 μM Ran	12400.15	35482.80	5731.14	6055.55
EK - 2500 nM Ca ²⁺ - 0 μM Ran	14940.82	51538.73	6366.24	7251.15
EK - 2500 nM Ca ²⁺ - 10 μM Ran	2860.49	2527.87	2816.21	2513.95
Peak I_{Na} Density (pA/pF)				
WT - 0 nM Ca ²⁺ - 0 μM Ran	446.63	597.28	463.00	604.67
WT - 0 nM Ca ²⁺ - 10 μM Ran	564.39	706.75	580.56	713.78
WT - 2500 nM Ca ²⁺ - 0 μM Ran	623.14	754.26	637.95	760.26
WT - 2500 nM Ca ²⁺ - 10 μM Ran	521.76	633.36	534.72	638.92
EK - 0 nM Ca ²⁺ - 0 μM Ran	270.93	288.18	272.97	288.90
EK - 0 nM Ca ²⁺ - 10 μM Ran	339.21	361.89	341.86	362.80
EK - 2500 nM Ca ²⁺ - 0 μM Ran	430.22	549.75	443.92	556.03
EK - 2500 nM Ca ²⁺ - 10 μM Ran	222.38	215.51	221.51	215.22
Late I_{Na} Density (pA/pF)				
WT - 0 nM Ca ²⁺ - 0 μM Ran	6.48	8.89	6.74	9.01
WT - 0 nM Ca ²⁺ - 10 μM Ran	11.26	19.76	12.09	20.26
WT - 2500 nM Ca ²⁺ - 0 μM Ran	11.08	11.77	11.17	11.80
WT - 2500 nM Ca ²⁺ - 10 μM Ran	8.17	10.02	8.38	10.11
EK - 0 nM Ca ²⁺ - 0 μM Ran	29.25	56.02	31.75	57.68
EK - 0 nM Ca ²⁺ - 10 μM Ran	4.15	4.58	4.20	4.60
EK - 2500 nM Ca ²⁺ - 0 μM Ran	11.61	12.41	11.71	12.45
EK - 2500 nM Ca ²⁺ - 10 μM Ran	13.12	18.37	13.69	18.65
Late Percent (%)				
WT - 0 nM Ca ²⁺ - 0 μM Ran	1.54	1.50	1.53	1.49
WT - 0 nM Ca ²⁺ - 10 μM Ran	2.27	3.71	2.41	3.79
WT - 2500 nM Ca ²⁺ - 0 μM Ran	2.80	2.91	2.81	2.92
WT - 2500 nM Ca ²⁺ - 10 μM Ran	1.18	1.30	1.19	1.31
EK - 0 nM Ca ²⁺ - 0 μM Ran	11.64	16.17	12.13	16.41
EK - 0 nM Ca ²⁺ - 10 μM Ran	0.92	1.00	0.93	1.00
EK - 2500 nM Ca ²⁺ - 0 μM Ran	1.86	1.69	1.84	1.69
EK - 2500 nM Ca ²⁺ - 10 μM Ran	3.94	4.96	4.05	5.01
GV-V_{1/2} (mV)				
WT - 0 nM Ca ²⁺ - 0 μM Ran	-44.27	-45.34	-44.40	-45.39
WT - 0 nM Ca ²⁺ - 10 μM Ran	-36.12	-33.96	-35.84	-33.87
WT - 2500 nM Ca ²⁺ - 0 μM Ran	-40.20	-39.68	-40.13	-39.66
WT - 2500 nM Ca ²⁺ - 10 μM Ran	-36.50	-34.66	-36.26	-34.58
EK - 0 nM Ca ²⁺ - 0 μM Ran	-29.04	-27.61	-28.86	-27.56
EK - 0 nM Ca ²⁺ - 10 μM Ran	-37.06	-37.39	-37.10	-37.40
EK - 2500 nM Ca ²⁺ - 0 μM Ran	-33.62	-32.25	-33.44	-32.19
EK - 2500 nM Ca ²⁺ - 10 μM Ran	-30.35	-29.25	-30.21	-29.21
GV-z				
WT - 0 nM Ca ²⁺ - 0 μM Ran	6.79	7.93	6.92	7.99
WT - 0 nM Ca ²⁺ - 10 μM Ran	4.84	4.71	4.82	4.71
WT - 2500 nM Ca ²⁺ - 0 μM Ran	6.59	7.49	6.70	7.53
WT - 2500 nM Ca ²⁺ - 10 μM Ran	5.55	6.11	5.62	6.13
EK - 0 nM Ca ²⁺ - 0 μM Ran	3.89	4.17	3.93	4.19
EK - 0 nM Ca ²⁺ - 10 μM Ran	4.68	5.21	4.75	5.23
EK - 2500 nM Ca ²⁺ - 0 μM Ran	4.36	4.78	4.41	4.80
EK - 2500 nM Ca ²⁺ - 10 μM Ran	4.28	4.78	4.34	4.80
SSFI-V_{1/2} (mV)				
Continued				

Condition	37°C (Q_{10})	41°C (Q_{10})	37°C (Arrhenius)	41°C (Arrhenius)
WT - 0 nM Ca ²⁺ - 0 μM Ran	-78.24	-75.70	-77.91	-75.59
WT - 0 nM Ca ²⁺ - 10 μM Ran	-81.49	-80.21	-81.32	-80.15
WT - 2500 nM Ca ²⁺ - 0 μM Ran	-77.46	-74.07	-77.02	-73.92
WT - 2500 nM Ca ²⁺ - 10 μM Ran	-81.11	-78.58	-80.79	-78.47
EK - 0 nM Ca ²⁺ - 0 μM Ran	-88.67	-85.79	-88.30	-85.67
EK - 0 nM Ca ²⁺ - 10 μM Ran	-92.87	-91.23	-92.66	-91.15
EK - 2500 nM Ca ²⁺ - 0 μM Ran	-95.62	-94.16	-95.43	-94.10
EK - 2500 nM Ca ²⁺ - 10 μM Ran	-93.54	-91.72	-93.31	-91.64
SSFI-z				
WT - 0 nM Ca ²⁺ - 0 μM Ran	-4.95	-5.26	-4.99	-5.27
WT - 0 nM Ca ²⁺ - 10 μM Ran	-4.02	-4.04	-4.02	-4.04
WT - 2500 nM Ca ²⁺ - 0 μM Ran	-4.41	-4.63	-4.44	-4.63
WT - 2500 nM Ca ²⁺ - 10 μM Ran	-4.02	-4.05	-4.03	-4.05
EK - 0 nM Ca ²⁺ - 0 μM Ran	-3.24	-3.31	-3.25	-3.32
EK - 0 nM Ca ²⁺ - 10 μM Ran	-3.21	-3.30	-3.22	-3.31
EK - 2500 nM Ca ²⁺ - 0 μM Ran	-3.31	-3.38	-3.32	-3.38
EK - 2500 nM Ca ²⁺ - 10 μM Ran	-2.90	-2.85	-2.89	-2.84
-50mV FI τ (ms)				
WT - 0 nM Ca ²⁺ - 0 μM Ran	2.04	1.77	2.00	1.76
WT - 0 nM Ca ²⁺ - 10 μM Ran	2.71	2.58	2.69	2.57
WT - 2500 nM Ca ²⁺ - 0 μM Ran	2.19	1.92	2.15	1.91
WT - 2500 nM Ca ²⁺ - 10 μM Ran	1.27	1.01	1.24	1.00
EK - 0 nM Ca ²⁺ - 0 μM Ran	0.80	0.69	0.78	0.69
EK - 0 nM Ca ²⁺ - 10 μM Ran	0.77	0.65	0.75	0.64
EK - 2500 nM Ca ²⁺ - 0 μM Ran	0.60	0.57	0.59	0.57
EK - 2500 nM Ca ²⁺ - 10 μM Ran	1.04	0.99	1.03	0.99
-30mV FI τ (ms)				
WT-0 nM Ca ²⁺ - 0 μM Ran	0.54	0.43	0.53	0.43
WT - 0 nM Ca ²⁺ - 10 μM Ran	0.61	0.52	0.60	0.52
WT - 2500 nM Ca ²⁺ - 0 μM Ran	0.36	0.26	0.35	0.25
WT - 2500 nM Ca ²⁺ - 10 μM Ran	0.51	0.42	0.50	0.42
EK - 0 nM Ca ²⁺ - 0 μM Ran	0.30	0.25	0.29	0.25
EK - 0 nM Ca ²⁺ - 10 μM Ran	0.26	0.21	0.25	0.21
EK - 2500 nM Ca ²⁺ - 0 μM Ran	0.23	0.20	0.23	0.20
EK - 2500 nM Ca ²⁺ - 10 μM Ran	0.31	0.27	0.31	0.27
-10mV FI τ (ms)				
WT - 0 nM Ca ²⁺ - 0 μM Ran	0.28	0.22	0.27	0.21
WT - 0 nM Ca ²⁺ - 10 μM Ran	0.30	0.25	0.29	0.25
WT - 2500 nM Ca ²⁺ - 0 μM Ran	0.21	0.16	0.20	0.15
WT-2500 nM Ca ²⁺ - 10 μM Ran	0.24	0.19	0.23	0.19
EK - 0 nM Ca ²⁺ - 0 μM Ran	0.20	0.16	0.19	0.16
EK - 0 nM Ca ²⁺ - 10 μM Ran	0.18	0.15	0.18	0.15
EK - 2500 nM Ca ²⁺ - 0 μM Ran	0.15	0.13	0.15	0.13
EK - 2500 nM Ca ²⁺ - 10 μM Ran	0.19	0.16	0.18	0.16
+10 mV FI τ (ms)				
WT - 0 nM Ca ²⁺ - 0 μM Ran	0.19	0.14	0.18	0.14
WT - 0 nM Ca ²⁺ - 10 μM Ran	0.20	0.16	0.19	0.16
WT - 2500 nM Ca ²⁺ - 0 μM Ran	0.16	0.12	0.16	0.12
WT - 2500 nM Ca ²⁺ - 10 μM Ran	0.16	0.13	0.16	0.12
EK - 0 nM Ca ²⁺ - 0 μM Ran	0.16	0.13	0.15	0.13
EK - 0 nM Ca ²⁺ - 10 μM Ran	0.15	0.12	0.14	0.12
EK - 2500 nM Ca ²⁺ - 0 μM Ran	0.12	0.10	0.12	0.10
EK - 2500 nM Ca ²⁺ - 10 μM Ran	0.15	0.12	0.14	0.12
1 Hz-y0				
WT - 0 nM Ca ²⁺ - 0 μM Ran	0.94	0.97	0.94	0.97
Continued				

Condition	37°C (Q_{10})	41°C (Q_{10})	37°C (Arrhenius)	41°C (Arrhenius)
WT - 0 nM Ca ²⁺ - 10 μM Ran	0.76	0.76	0.76	0.76
WT - 2500 nM Ca ²⁺ - 0 μM Ran	0.90	0.93	0.90	0.93
WT - 2500 nM Ca ²⁺ - 10 μM Ran	0.83	0.85	0.84	0.85
EK - 0 nM Ca ²⁺ - 0 μM Ran	0.86	0.92	0.87	0.92
EK - 0 nM Ca ²⁺ - 10 μM Ran	0.83	0.91	0.84	0.92
EK - 2500 nM Ca ²⁺ - 0 μM Ran	0.92	0.97	0.92	0.97
EK - 2500 nM Ca ²⁺ - 10 μM Ran	0.83	0.90	0.84	0.91
1 Hz-τ1 (s)				
WT - 0 nM Ca ²⁺ - 0 μM Ran	5.34	6.15	5.43	6.18
WT - 0 nM Ca ²⁺ - 10 μM Ran	6.34	7.76	6.51	7.83
WT - 2500 nM Ca ²⁺ - 0 μM Ran	42.49	65.65	44.88	66.93
WT - 2500 nM Ca ²⁺ - 10 μM Ran	2.23	1.65	2.15	1.63
EK - 0 nM Ca ²⁺ - 0 μM Ran	8.14	10.28	8.38	10.38
EK - 0 nM Ca ²⁺ - 10 μM Ran	2.22	2.01	2.19	2.00
EK - 2500 nM Ca ²⁺ - 0 μM Ran	25.75	50.72	28.04	52.25
EK - 2500 nM Ca ²⁺ - 10 μM Ran	1.22	0.77	1.15	0.75
1 Hz-τ2 (s)				
WT - 0 nM Ca ²⁺ - 0 μM Ran	37.43	35.07	37.13	34.97
WT - 0 nM Ca ²⁺ - 10 μM Ran	86.46	129.96	91.00	132.31
WT - 2500 nM Ca ²⁺ - 0 μM Ran	50.52	40.70	49.16	40.30
WT - 2500 nM Ca ²⁺ - 10 μM Ran	81.65	104.69	84.25	105.85
EK - 0 nM Ca ²⁺ - 0 μM Ran	68.52	68.34	68.50	68.33
EK - 0 nM Ca ²⁺ - 10 μM Ran	82.26	87.65	82.91	87.89
EK - 2500 nM Ca ²⁺ - 0 μM Ran	79.80	102.18	82.29	103.26
EK - 2500 nM Ca ²⁺ - 10 μM Ran	43.43	37.52	42.64	37.27
3 Hz-γ0				
WT - 0 nM Ca ²⁺ - 0 μM Ran	0.90	0.99	0.91	1.00
WT - 0 nM Ca ²⁺ - 10 μM Ran	0.69	0.75	0.70	0.75
WT - 2500 nM Ca ²⁺ - 0 μM Ran	0.83	0.88	0.84	0.88
WT - 2500 nM Ca ²⁺ - 10 μM Ran	0.63	0.65	0.63	0.66
EK - 0 nM Ca ²⁺ - 0 μM Ran	0.79	0.82	0.79	0.83
EK - 0 nM Ca ²⁺ - 10 μM Ran	0.57	0.60	0.57	0.60
EK - 2500 nM Ca ²⁺ - 0 μM Ran	0.76	0.78	0.76	0.78
EK - 2500 nM Ca ²⁺ - 10 μM Ran	0.68	0.76	0.69	0.76
3 Hz-τ1 (s)				
WT - 0 nM Ca ²⁺ - 0 μM Ran	2.97	3.29	3.01	3.30
WT - 0 nM Ca ²⁺ - 10 μM Ran	0.70	0.46	0.67	0.46
WT - 2500 nM Ca ²⁺ - 0 μM Ran	1.38	1.28	1.36	1.27
WT - 2500 nM Ca ²⁺ - 10 μM Ran	0.98	0.93	0.97	0.92
EK - 0 nM Ca ²⁺ - 0 μM Ran	3.07	3.69	3.14	3.72
EK - 0 nM Ca ²⁺ - 10 μM Ran	1.47	1.29	1.45	1.28
EK - 2500 nM Ca ²⁺ - 0 μM Ran	2.27	2.01	2.24	2.00
EK - 2500 nM Ca ²⁺ - 10 μM Ran	0.84	0.58	0.81	0.57
3 Hz-τ2 (s)				
WT - 0 nM Ca ²⁺ - 0 μM Ran	14.24	10.80	13.75	10.66
WT - 0 nM Ca ²⁺ - 10 μM Ran	15.28	13.72	15.08	13.65
WT - 2500 nM Ca ²⁺ - 0 μM Ran	39.52	40.39	39.63	40.43
WT - 2500 nM Ca ²⁺ - 10 μM Ran	20.81	26.32	21.43	26.60
EK - 0 nM Ca ²⁺ - 0 μM Ran	54.26	61.55	55.14	61.90
EK - 0 nM Ca ²⁺ - 10 μM Ran	31.12	36.95	31.81	37.24
EK - 2500 nM Ca ²⁺ - 0 μM Ran	43.81	68.26	46.41	69.75
EK - 2500 nM Ca ²⁺ - 10 μM Ran	5.29	4.15	5.13	4.11

Table 6. Values at 37°C and 41°C based on Q_{10} and Arrhenius Calculations.

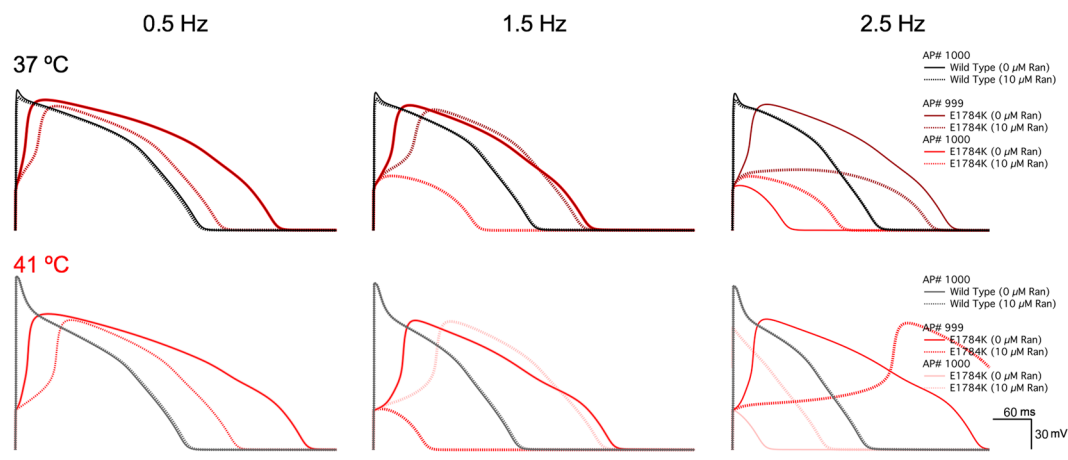


Figure 8. Endocardial action potential simulations. AP simulations are plotted against time (*inset* is shown in bottom right corner) at 37 °C and 41 °C. The last two AP beats were plotted in E1784K to show alternans-induction. Simulations only included therapeutic concentrations of Ranolazine (10 μM).

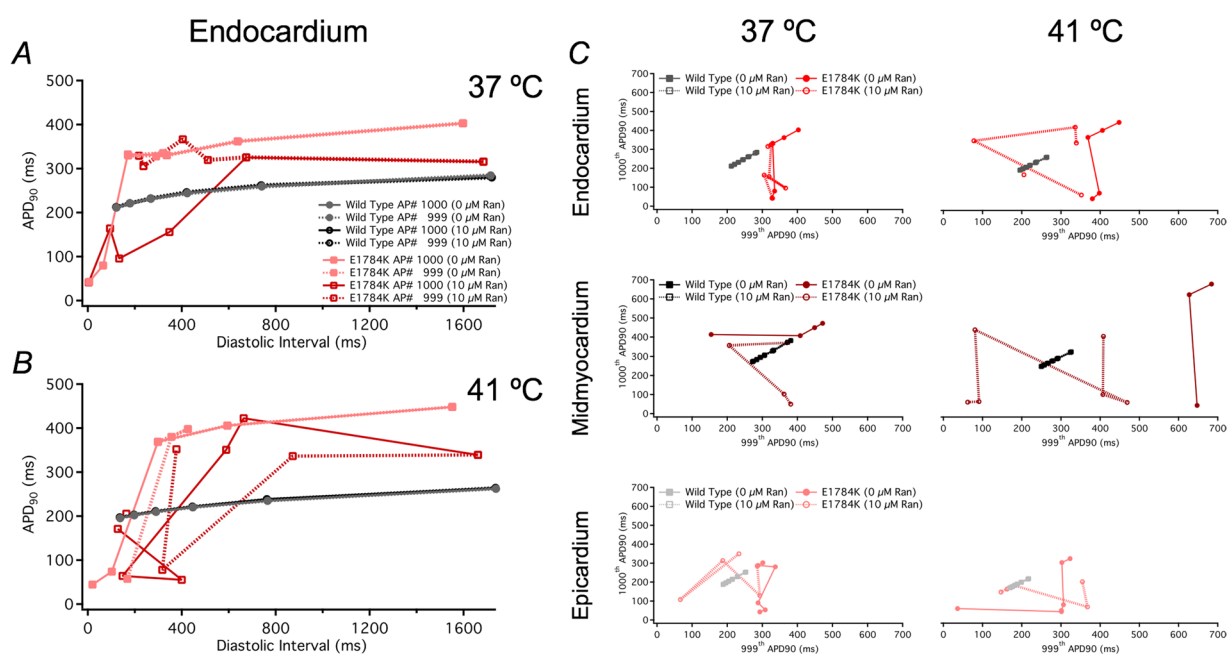


Figure 9. Cardiac electrical restitution properties. Panel A,B shows the endocardial ERC curves at 37 °C and 41 °C. Panels C shows plots of the last two AP beats to determine alternans-induction in the three myocardial cells at 37 °C and 41 °C.

$$\ln(k) = \ln(A) - (E_a/R) \times (1/T) \quad (7)$$

where k is the rate constant, steady-state midpoint, or slope, A is the pre-exponential factor, E_a is the activation energy, R is the universal gas constant, and T is temperature in °K.

Myocardial Action Potential (AP) Modeling. Simulations. Action potentials were simulated using a modified version of the O'Hara Rudy (ORD) model at 37 °C and 41 °C programmed in Matlab⁸⁷. The sodium data was extrapolated to physiological and febrile temperatures Q_{10} values for WT and E1784K at 0 μM and 10 μM Ranolazine. The maximal G_{Na} density was 150 mS/μF in all conditions simulated. We modified the gating I_{Na} parameters data in accordance with our biophysical data for the various conditions. The GV and SSFI midpoints and slopes were extrapolated to 37 °C and 41 °C and normalized to the original ORD parameters. The phosphorylated steady-state fast inactivation midpoints in all channel variants were equally hyperpolarized by 6.2 mV. Late I_{Na} density was normalized to the original ORD value and multiplied by the percentage of late to peak I_{Na} calculated above.

Condition	Voltage Error (mV)	N
WT - 22 °C - 0 nM Ca ²⁺ - 0 μM Ran	3.52 ± 0.97	9
WT - 22 °C - 0 nM Ca ²⁺ - 10 μM Ran	7.83 ± 1.47	8
WT - 22 °C - 0 nM Ca ²⁺ - 100 μM Ran	5.70 ± 2.05	6
WT - 22 °C - 2500 nM Ca ²⁺ - 0 μM Ran	4.89 ± 1.29	9
WT - 22 °C - 2500 nM Ca ²⁺ - 10 μM Ran	6.54 ± 1.30	11
WT - 22 °C - 2500 nM Ca ²⁺ - 100 μM Ran	3.12 ± 0.88	10
WT - 34 °C - 0 nM Ca ²⁺ - 0 μM Ran	8.35 ± 1.56	11
WT - 34 °C - 0 nM Ca ²⁺ - 10 μM Ran	9.08 ± 1.32	9
WT - 34 °C - 0 nM Ca ²⁺ - 100 μM Ran	7.18 ± 1.16	19
WT - 34 °C - 2500 nM Ca ²⁺ - 0 μM Ran	8.64 ± 0.98	7
WT - 34 °C - 2500 nM Ca ²⁺ - 10 μM Ran	8.53 ± 1.79	9
WT - 34 °C - 2500 nM Ca ²⁺ - 100 μM Ran	8.14 ± 1.57	6
EK - 22 °C - 0 nM Ca ²⁺ - 0 μM Ran	4.41 ± 0.65	19
EK - 22 °C - 0 nM Ca ²⁺ - 10 μM Ran	5.99 ± 1.22	10
EK - 22 °C - 0 nM Ca ²⁺ - 100 μM Ran	4.28 ± 0.72	14
EK - 22 °C - 2500 nM Ca ²⁺ - 0 μM Ran	3.01 ± 0.71	6
EK - 22 °C - 2500 nM Ca ²⁺ - 10 μM Ran	4.49 ± 1.04	9
EK - 22 °C - 2500 nM Ca ²⁺ - 100 μM Ran	4.63 ± 1.21	10
EK - 34 °C - 0 nM Ca ²⁺ - 0 μM Ran	6.50 ± 1.09	19
EK - 34 °C - 0 nM Ca ²⁺ - 10 μM Ran	6.74 ± 1.73	10
EK - 34 °C - 0 nM Ca ²⁺ - 100 μM Ran	5.52 ± 0.98	12
EK - 34 °C - 2500 nM Ca ²⁺ - 0 μM Ran	5.63 ± 1.32	8
EK - 34 °C - 2500 nM Ca ²⁺ - 10 μM Ran	8.95 ± 1.97	8
EK - 34 °C - 2500 nM Ca ²⁺ - 100 μM Ran	3.67 ± 0.69	11

Table 7. Voltage Error.

To model the calcium-dependence of our late I_{Na} data, we fit the biophysical parameters extrapolated to 37 °C and 41 °C with a Hill equation:

$$Z = Y_0 + (Y_M - Y_0)/(1 + (X_{1/2}/X)^b) \quad (8)$$

where Z is the biophysical parameter of interest, Y_0 is the minimum value, Y_M is the maximum value, $X_{1/2}$ is the midpoint of the curve, X is the intracellular cytosolic calcium, b is the rate.

Subspace calcium was not accounted for due to the lack of experimental data. Thus, the modified ORd model is a dynamic simulation of the calcium-induced shifts which are observed with increasing intracellular calcium levels as a function of pacing frequency, comprising the positive staircase phenomenon^{88,89}.

Simulations at febrile temperature (41 °C) included modifications to the major ionic currents, I_{Kto} ⁹⁰, I_{CaL} ^{91,92}, I_{Kr} ⁹³, and I_{Ks} ⁹⁴, in the ORd model based on previously published Q_{10} values.

Simulations were run on endocardial, midmyocardial, and epicardial ventricular myocytes using a 0.5 ms stimulus pulse with an amplitude of $-80 \mu A/\mu F$. The stimulus protocol was designed to step up the frequency gradually from 0.5 Hz to 2.5 Hz, with a 1000 beats per frequency step to ensure attainment of steady-state.

Analysis. Analysis of APs only included those that fully recovered and were restored to baseline. Action potential duration (APD) was measured at 90% of repolarization by multiplying the resting membrane potential (RMP) value, prior to the current stimulus pulse, by 0.9. The APD_{90} of the final two beats in the frequency step were plotted versus the diastolic interval ($DI = BCL - APD_{90}$), where BCL is the basic cycle length, creating electrical restitution curves.

Data Availability. All data generated or analysed during this study are included in this published article.

References

1. Bezzina, C. *et al.* A Single Na⁺ Channel Mutation Causing Both Long-QT and Brugada Syndromes. *Circ. Res.* **85**, 1206–1213 (1999).
2. Rivolta, I. Inherited Brugada and Long QT-3 Syndrome Mutations of a Single Residue of the Cardiac Sodium Channel Confer Distinct Channel and Clinical Phenotypes. *J. Biol. Chem.* **276**, 30623–30630 (2001).
3. Kapplinger, J. D. *et al.* An international compendium of mutations in the SCN5A-encoded cardiac sodium channel in patients referred for Brugada syndrome genetic testing. *Heart Rhythm Off. J. Heart Rhythm Soc.* **7**, 33–46 (2010).
4. Antzelevitch, C., Brugada, P., Brugada, J. & Brugada, R. Brugada syndrome: from cell to bedside. *Curr. Probl. Cardiol.* **30**, 9–54 (2005).
5. Shimizu, W. & Antzelevitch, C. Differential effects of beta-adrenergic agonists and antagonists in LQT1, LQT2 and LQT3 models of the long QT syndrome. *J. Am. Coll. Cardiol.* **35**, 778–786 (2000).
6. Baroudi, G. & Chahine, M. Biophysical phenotypes of SCN5A mutations causing long QT and Brugada syndromes. *FEBS Lett.* **487**, 224–228 (2000).

7. Dumaine, R. *et al.* Multiple mechanisms of Na⁺ channel-linked long-QT syndrome. *Circ. Res.* **78**, 916–924 (1996).
8. Sun, A. Y. *et al.* The S1103Y cardiac sodium channel variant is associated with ICD events in African Americans with heart failure and reduced ejection fraction. *Circ. Cardiovasc. Genet.* CIRCGENETICS-110 (2011).
9. Baroudi, G., Acharfi, S., Larouche, C. & Chahine, M. Expression and intracellular localization of an SCN5A double mutant R1232W/T1620M implicated in Brugada syndrome. *Circ. Res.* **90**, E11–16 (2002).
10. Makita, N., Mochizuki, N. & Tsutsui, H. Absence of a trafficking defect in R1232W/T1620M, a double SCN5A mutant responsible for Brugada syndrome. *Circ. J. Off. J. Jpn. Circ. Soc.* **72**, 1018–1019 (2008).
11. Chandra, R., Starmer, C. F. & Grant, A. O. Multiple effects of KPQ deletion mutation on gating of human cardiac Na⁺ channels expressed in mammalian cells. *Am. J. Physiol.* **274**, H1643–1654 (1998).
12. Wei, J. *et al.* Congenital Long-QT Syndrome Caused by a Novel Mutation in a Conserved Acidic Domain of the Cardiac Na⁺ Channel. *Circulation* **99**, 3165–3171 (1999).
13. Groenewegen, W. A. *et al.* A novel LQT3 mutation implicates the human cardiac sodium channel domain IVS6 in inactivation kinetics. *Cardiovasc. Res.* **57**, 1072–1078 (2003).
14. Moreau, A. *et al.* Sodium overload due to a persistent current that attenuates the arrhythmogenic potential of a novel LQT3 mutation. *Front. Pharmacol.* **4**, 126 (2013).
15. Kwon, H. W. *et al.* Long QT syndrome and dilated cardiomyopathy with SCN5A p.R1193Q polymorphism: cardioverter-defibrillator implantation at 27 months. *Pacing Clin. Electrophysiol.* *PACE* **35**, e243–246 (2012).
16. Bankston, J. R. *et al.* A novel LQT-3 mutation disrupts an inactivation gate complex with distinct rate-dependent phenotypic consequences. *Channels Austin Tex* **1**, 273–280 (2007).
17. Veldkamp, M. W. *et al.* UltraRapid Communication. *Circ Res* **86**, e91–e97 (2000).
18. Mok, N.-S. *et al.* A newly characterized SCN5A mutation underlying Brugada syndrome unmasked by hyperthermia. *J. Cardiovasc. Electrophysiol.* **14**, 407–411 (2003).
19. Hwang, H. W. *et al.* R1193Q of SCN5A, a Brugada and long QT mutation, is a common polymorphism in Han Chinese. *J. Med. Genet.* **42**, e7; author reply e8 (2005).
20. Wang, D. W., Makita, N., Kitabatake, A., Balsler, J. R. & George, A. L. Enhanced Na⁺ channel intermediate inactivation in Brugada syndrome. *Circ. Res.* **87**, e37–e43 (2000).
21. Postema, P. G. *et al.* Founder mutations in the Netherlands: SCN5a 1795insD, the first described arrhythmia overlap syndrome and one of the largest and best characterised families worldwide. *Neth. Heart J. Mon. J. Neth. Soc. Cardiol. Neth. Heart Found.* **17**, 422–428 (2009).
22. Makita, N. *et al.* The E1784K mutation in SCN5A is associated with mixed clinical phenotype of type 3 long QT syndrome. *J. Clin. Invest.* <https://doi.org/10.1172/JCI34057> (2008).
23. Huang, H., Zhao, J., Barrane, F.-Z., Champagne, J. & Chahine, M. Nav1.5/R1193Q polymorphism is associated with both long QT and Brugada syndromes. *Can. J. Cardiol.* **22**, 309–313 (2006).
24. Chen, J. *et al.* Cardiac sodium channel mutation associated with epinephrine-induced QT prolongation and sinus node dysfunction. *Heart Rhythm Off. J. Heart Rhythm Soc.* <https://doi.org/10.1016/j.hrthm.2015.08.021> (2015).
25. Splawski, I. *et al.* Spectrum of mutations in long-QT syndrome genes. KVLQT1, HERG, SCN5A, KCNE1, and KCNE2. *Circulation* **102**, 1178–1185 (2000).
26. Tester, D. J., Will, M. L., Haglund, C. M. & Ackerman, M. J. Compendium of cardiac channel mutations in 541 consecutive unrelated patients referred for long QT syndrome genetic testing. *Heart Rhythm* **2**, 507–517 (2005).
27. Takahashi, K. *et al.* High prevalence of the SCN5A E1784K mutation in school children with long QT syndrome living on the Okinawa islands. *Circ. J. Off. J. Jpn. Circ. Soc.* **78**, 1974–1979 (2014).
28. Deschênes, I. *et al.* Electrophysiological characterization of SCN5A mutations causing long QT (E1784K) and Brugada (R1512W and R1432G) syndromes. *Cardiovasc. Res.* **46**, 55–65 (2000).
29. Sumitomo, N. E1784K mutation in SCN5A and overlap syndrome. *Circ. J. Off. J. Jpn. Circ. Soc.* **78**, 1839–1840 (2014).
30. Mantegazza, M., Yu, F. H., Catterall, W. A. & Scheuer, T. Role of the C-terminal domain in inactivation of brain and cardiac sodium channels. *Proc. Natl. Acad. Sci. USA* **98**, 15348–15353 (2001).
31. Chagot, B., Potet, F., Balsler, J. R. & Chazin, W. J. Solution NMR Structure of the C-terminal EF-hand Domain of Human Cardiac Sodium Channel Nav1.5. *J. Biol. Chem.* **284**, 6436–6445 (2009).
32. Cormier, J. W., Rivolta, I., Tateyama, M., Yang, A.-S. & Kass, R. S. Secondary Structure of the Human Cardiac Na⁺ Channel C Terminus: Evidence For a Role of Helical Structures In Modulation of Channel Inactivation. *J. Biol. Chem.* **277**, 9233–9241 (2002).
33. Glaaser, I. W., Bankston, J. R., Liu, H., Tateyama, M. & Kass, R. S. A carboxyl-terminal hydrophobic interface is critical to sodium channel function. Relevance to inherited disorders. *J. Biol. Chem.* **281**, 24015–24023 (2006).
34. Kim, J. *et al.* Calmodulin Mediates Ca²⁺ Sensitivity of Sodium Channels. *J. Biol. Chem.* **279**, 45004–45012 (2004).
35. Glaaser, I. W. *et al.* Perturbation of sodium channel structure by an inherited Long QT Syndrome mutation. *Nat. Commun.* **3**, 706 (2012).
36. Motoike, H. K. The Na⁺ Channel Inactivation Gate Is a Molecular Complex: A Novel Role of the COOH-terminal Domain. *J. Gen. Physiol.* **123**, 155–165 (2004).
37. Abdelsayed, M. *et al.* Differential calcium sensitivity in Nav_v1.5 mixed syndrome mutants: Calcium and mixed syndrome mutants. *J. Physiol.* <https://doi.org/10.1113/JP274536> (2017).
38. Mori, M., Konno, T., Morii, T., Nagayama, K. & Imoto, K. Regulatory interaction of sodium channel IQ-motif with calmodulin C-terminal lobe. *Biochem. Biophys. Res. Commun.* **307**, 290–296 (2003).
39. Yan, H., Wang, C., Marx, S. O. & Pitt, G. S. Calmodulin limits pathogenic Na⁺ channel persistent current. *J. Gen. Physiol.* **149**, 277–293 (2017).
40. Van Petegem, F., Lobo, P. A. & Ahern, C. A. Seeing the Forest through the Trees: towards a Unified View on Physiological Calcium Regulation of Voltage-Gated Sodium Channels. *Biophys. J.* **103**, 2243–2251 (2012).
41. Abdelsayed, M., Peters, C. H. & Ruben, P. C. Differential thermosensitivity in mixed syndrome cardiac sodium channel mutants. *J. Physiol.* <https://doi.org/10.1113/JP270139> (2015).
42. Peters, C. H., Abdelsayed, M. & Ruben, P. C. Triggers for arrhythmogenesis in the Brugada and long QT 3 syndromes. *Prog. Biophys. Mol. Biol.* **120**, 77–88 (2016).
43. Peters, C. H., Yu, A., Zhu, W., Silva, J. R. & Ruben, P. C. Depolarization of the conductance-voltage relationship in the Nav1.5 mutant, E1784K, is due to altered fast inactivation. *PLOS ONE* **12**, e0184605 (2017).
44. Potet, F., Beckermann, T. M., Kunic, J. D. & George, A. L. Intracellular Calcium Attenuates Late Current Conducted by Mutant Human Cardiac Sodium Channels. *Circ. Arrhythm. Electrophysiol.* <https://doi.org/10.1161/CIRCEP.115.002760> (2015).
45. Antzelevitch, C. Electrophysiological Effects of Ranolazine, a Novel Antianginal Agent With Antiarrhythmic Properties. *Circulation* **110**, 904–910 (2004).
46. Antzelevitch, C. *et al.* Electrophysiologic properties and antiarrhythmic actions of a novel antianginal agent. *J. Cardiovasc. Pharmacol. Ther.* **9**(Suppl 1), S65–83 (2004).
47. Sossalla, S. *et al.* Ranolazine improves diastolic dysfunction in isolated myocardium from failing human hearts—Role of late sodium current and intracellular ion accumulation. *J. Mol. Cell. Cardiol.* **45**, 32–43 (2008).
48. Sokolov, S., Peters, C. H., Rajamani, S. & Ruben, P. C. Proton-dependent inhibition of the cardiac sodium channel Nav1.5 by ranolazine. *Front. Pharmacol.* **4**, (2013).

49. Huang, H., Priori, S. G., Napolitano, C., O'Leary, M. E. & Chahine, M. Y1767C, a novel SCN5A mutation, induces a persistent Na⁺ current and potentiates ranolazine inhibition of Nav1.5 channels. *AJP Heart Circ. Physiol.* **300**, H288–H299 (2011).
50. Moss, A. J. *et al.* Ranolazine Shortens Repolarization in Patients with Sustained Inward Sodium Current Due to Type-3 Long-QT Syndrome. *J. Cardiovasc. Electrophysiol.* **19**, 1289–1293 (2008).
51. Rajamani, S., El-Bizri, N., Shryock, J. C., Makielski, J. C. & Belardinelli, L. Use-dependent block of cardiac late Na⁽⁺⁾ current by ranolazine. *Heart Rhythm Off. J. Heart Rhythm Soc.* **6**, 1625–1631 (2009).
52. Fredj, S., Sampson, K. J., Liu, H. & Kass, R. S. Molecular basis of ranolazine block of LQT-3 mutant sodium channels: evidence for site of action. *Br. J. Pharmacol.* **148**, 16–24 (2006).
53. Belardinelli, L. The mechanism of ranolazine action to reduce ischemia-induced diastolic dysfunction. *Eur. Heart J. Suppl.* **8**, A10–A13 (2006).
54. Peters, C., Sokolov, S., Rajamani, S. & Ruben, P. Effects of the antianginal drug, ranolazine, on the brain sodium channel Na_v1.2 and its modulation by extracellular protons: Effects of ranolazine on Nav1.2 in normal and low extracellular pH. *Br. J. Pharmacol.* **169**, 704–716 (2013).
55. Lipkind, G. M. & Fozzard, H. A. Molecular Model of Anticonvulsant Drug Binding to the Voltage-Gated Sodium Channel Inner Pore. *Mol. Pharmacol.* **78**, 631–638 (2010).
56. Nolasco, J. B. & Dahlen, R. W. A graphic method for the study of alternation in cardiac action potentials. *J. Appl. Physiol.* **25**, 191–196 (1968).
57. Franz, M. R. The Electrical Restitution Curve Revisited: Steep or Flat Slope-Which is Better? *J. Cardiovasc. Electrophysiol.* **14**, S140–S147 (2003).
58. Jordan, P. N. & Christini, D. J. Determining the effects of memory and action potential duration alternans on cardiac restitution using a constant-memory restitution protocol. *Physiol. Meas.* **25**, 1013–1024 (2004).
59. Ragsdale, D. S., McPhee, J. C., Scheuer, T. & Catterall, W. A. Common molecular determinants of local anesthetic, antiarrhythmic, and anticonvulsant block of voltage-gated Na⁺ channels. *Proc. Natl. Acad. Sci. USA* **93**, 9270–9275 (1996).
60. Vilin, Y. Y., Peters, C. H. & Ruben, P. C. Acidosis Differentially Modulates Inactivation in Nav1.2, Nav1.4, and Nav1.5 Channels. *Front. Pharmacol.* **3**, (2012).
61. Jones, D. K., Peters, C. H., Tolhurst, S. A., Claydon, T. W. & Ruben, P. C. Extracellular Proton Modulation of the Cardiac Voltage-Gated Sodium Channel, Nav1.5. *Biophys. J.* **101**, 2147–2156 (2011).
62. Chorin, E. *et al.* Ranolazine for Congenital Long-QT Syndrome Type III: Experimental and Long-Term Clinical Data. *Circ. Arrhythm. Electrophysiol.* **9**, (2016).
63. Murray, K. T., Anno, T., Bennett, P. B. & Hondeghem, L. M. Voltage clamp of the cardiac sodium current at 37 degrees C in physiologic solutions. *Biophys. J.* **57**, 607 (1990).
64. Ruff, R. L. Effects of temperature on slow and fast inactivation of rat skeletal muscle Na⁽⁺⁾ channels. *Am. J. Physiol.* **277**, C937–947 (1999).
65. Hille, B. Local anesthetics: hydrophilic and hydrophobic pathways for the drug-receptor reaction. *J. Gen. Physiol.* **69**, 497–515 (1977).
66. Tikhonov, D. B. & Zhorov, B. S. Mechanism of sodium channel block by local anesthetics, antiarrhythmics, and anticonvulsants. *J. Gen. Physiol.* **149**, 465–481 (2017).
67. Shen, H. *et al.* Structure of a eukaryotic voltage-gated sodium channel at near-atomic resolution. *Science* **355**, eaal4326 (2017).
68. Ahuja, S. *et al.* Structural basis of Nav1.7 inhibition by an isoform-selective small-molecule antagonist. *Science* **350**, aac5464–aac5464 (2015).
69. Capes, D. L., Goldschen-Ohm, M. P., Arcisio-Miranda, M., Bezanilla, F. & Chanda, B. Domain IV voltage-sensor movement is both sufficient and rate limiting for fast inactivation in sodium channels. *J. Gen. Physiol.* **142**, 101–112 (2013).
70. Kühn, F. J. & Greeff, N. G. Movement of voltage sensor S4 in domain 4 is tightly coupled to sodium channel fast inactivation and gating charge immobilization. *J. Gen. Physiol.* **114**, 167–183 (1999).
71. Shah, V. N. *et al.* Calcium-dependent regulation of the voltage-gated sodium channel hH1: intrinsic and extrinsic sensors use a common molecular switch. *Proc. Natl. Acad. Sci. USA* **103**, 3592–3597 (2006).
72. Sarhan, M. F., Van Petegem, F. & Ahern, C. A. A Double Tyrosine Motif in the Cardiac Sodium Channel Domain III-IV Linker Couples Calcium-dependent Calmodulin Binding to Inactivation Gating. *J. Biol. Chem.* **284**, 33265–33274 (2009).
73. Sarhan, M. F., Tung, C.-C., Van Petegem, F. & Ahern, C. A. Crystallographic basis for calcium regulation of sodium channels. *Proc. Natl. Acad. Sci.* **109**, 3558–3563 (2012).
74. Ben-Johny, M. *et al.* Conservation of Ca²⁺/Calmodulin Regulation across Na and Ca²⁺ Channels. *Cell* **157**, 1657–1670 (2014).
75. Pitt, G. S. & Lee, S.-Y. Current view on regulation of voltage-gated sodium channels by calcium and auxiliary proteins. *Protein Sci.* <https://doi.org/10.1002/pro.2960> (2016).
76. Petegem, F. V., Chatelain, F. C. & Minor, D. L. Insights into voltage-gated calcium channel regulation from the structure of the CaV1.2 IQ domain–Ca²⁺/calmodulin complex. *Nat. Struct. Mol. Biol.* **12**, 1108–1115 (2005).
77. Ben-Johny, M. & Yue, D. T. Calmodulin regulation (calmodulation) of voltage-gated calcium channels. *J. Gen. Physiol.* **143**, 679–692 (2014).
78. Lukas, A. & Antzelevitch, C. Phase 2 reentry as a mechanism of initiation of circus movement reentry in canine epicardium exposed to simulated ischemia. *Cardiovasc. Res.* **32**, 593–603 (1996).
79. Rivera-Fernández, R. *et al.* Prolonged QT interval in ST-elevation myocardial infarction and mortality: new prognostic scale with QT, Killip and age. *J. Cardiovasc. Med. Hagerstown Md* <https://doi.org/10.2459/JCM.0000000000000015> (2014).
80. Schwartz, P. J. *et al.* Long QT syndrome patients with mutations of the SCN5A and HERG genes have differential responses to Na⁺ channel blockade and to increases in heart rate. Implications for gene-specific therapy. *Circulation* **92**, 3381–3386 (1995).
81. Di Diego, J. M., Sun, Z. Q. & Antzelevitch, C. I(to) and action potential notch are smaller in left vs. right canine ventricular epicardium. *Am. J. Physiol.* **271**, H548–561 (1996).
82. Bordoli, L. *et al.* Protein structure homology modeling using SWISS-MODEL workspace. *Nat. Protoc.* **4**, 1–13 (2008).
83. Morris, G. M. *et al.* AutoDock4 and AutoDockTools4: Automated docking with selective receptor flexibility. *J. Comput. Chem.* **30**, 2785–2791 (2009).
84. Black, D., Tran, Q.-K. & Persechini, A. Monitoring the total available calmodulin concentration in intact cells over the physiological range in free Ca²⁺. *Cell Calcium* **35**, 415–425 (2004).
85. Steenbergen, C., Murphy, E., Levy, L. & London, R. E. Elevation in cytosolic free calcium concentration early in myocardial ischemia in perfused rat heart. *Circ. Res.* **60**, 700–707 (1987).
86. Kirschenlohr, H. L., Grace, A. A., Vandenberg, J. I., Metcalfe, J. C. & Smith, G. A. Estimation of systolic and diastolic free intracellular Ca²⁺ by titration of Ca²⁺ buffering in the ferret heart. *Biochem. J.* **346**(Pt 2), 385–391 (2000).
87. O'Hara, T., Virág, L., Varró, A. & Rudy, Y. Simulation of the Undiseased Human Cardiac Ventricular Action Potential: Model Formulation and Experimental Validation. *PLoS Comput. Biol.* **7**, e1002061 (2011).
88. Kort, A. A., Capogrossi, M. C. & Lakatta, E. G. Frequency, amplitude, and propagation velocity of spontaneous Ca⁺⁺-dependent contractile waves in intact adult rat cardiac muscle and isolated myocytes. *Circ. Res.* **57**, 844–855 (1985).
89. Song, L. S. *et al.* Beta-Adrenergic stimulation synchronizes intracellular Ca⁽²⁺⁾ release during excitation-contraction coupling in cardiac myocytes. *Circ. Res.* **88**, 794–801 (2001).
90. Yang, F. & Zheng, J. High temperature sensitivity is intrinsic to voltage-gated potassium channels. *eLife* **3**, e03255 (2014).

91. ten Tusscher, K. H. W. J. A model for human ventricular tissue. *AJP Heart Circ. Physiol.* **286**, H1573–H1589 (2003).
92. Radzicki, D. *et al.* Temperature-Sensitive Cav1.2 Calcium Channels Support Intrinsic Firing of Pyramidal Neurons and Provide a Target for the Treatment of Febrile Seizures. *J. Neurosci.* **33**, 9920–9931 (2013).
93. Mauerhöfer, M. & Bauer, C. K. Effects of Temperature on Heteromeric Kv11.1a/1b and Kv11.3 Channels. *Biophys. J.* **111**, 504–523 (2016).
94. Seebohm, G., Lerche, C., Busch, A. E. & Bachmann, A. Dependence of I_{Ks} biophysical properties on the expression system. *Pflügers Arch. Eur. J. Physiol.* **442**, 891–895 (2001).

Acknowledgements

We thank Dr. Elizabeth M. Cherry for helping in A.P. simulation analysis. We are also grateful to both Mr. Colin Peters and Mr. Mohammed-Reza Ghovanloo for their valuable input and support. P.R. and M.A. receive funding from Simon Fraser University, the Natural Sciences and Engineering Research Council of Canada, and the Canadian Foundation for Innovation.

Author Contributions

M.A. and co-author collected, assembled, analyzed, and interpreted the data, designed the experiments, and drafted the manuscript. M.R. collected, assembled, and analyzed data. P.C.R. conceived the experiments and revised the manuscript critically for important intellectual content. All authors approved the final version of the manuscript and qualify for authorship.

Additional Information

Competing Interests: The authors declare no competing interests.

Publisher's note: Springer Nature remains neutral with regard to jurisdictional claims in published maps and institutional affiliations.



Open Access This article is licensed under a Creative Commons Attribution 4.0 International License, which permits use, sharing, adaptation, distribution and reproduction in any medium or format, as long as you give appropriate credit to the original author(s) and the source, provide a link to the Creative Commons license, and indicate if changes were made. The images or other third party material in this article are included in the article's Creative Commons license, unless indicated otherwise in a credit line to the material. If material is not included in the article's Creative Commons license and your intended use is not permitted by statutory regulation or exceeds the permitted use, you will need to obtain permission directly from the copyright holder. To view a copy of this license, visit <http://creativecommons.org/licenses/by/4.0/>.

© The Author(s) 2018